2009-01-01

Hybrid Method: Algebraic/inverse Radon Transform For Region Of Interest Reconstruction Of Computed Tomography Images

Marco A. Barrera
University of Texas at El Paso, still_en@yahoo.com

HYBRID METHOD: ALGEBRAIC/INVERSE RADON TRANSFORM FOR REGION OF INTEREST RECONSTRUCTION OF COMPUTED TOMOGRAPHY IMAGES.

MARCO ANTONIO BARRERA CRUZ

Department of Physics

APPROVED:

_____
Marian-Mihai Manciu, Ph.D. Chair

_____
Norris J. Parks, Ph. D.

_____
William G. Durrer, Ph.D.

_____
Robert G. Waggener, Ph.D.

_____
Patricia D.Witherspoon, Ph.D.
Dean of Graduate School.

DEDICATION

To all who has put faith on me and believed in me...

To my mother: I would like to say thank you because she has given me a good set of wings.

My brothers and my nephew: Because they are my arms to keep fighting.

My friends: Because we will laugh about all this work again!.

... Sit Nomen Domini Benedictum

HYBRID METHOD: ALGEBRAIC/INVERSE RADON TRANSFORM FOR REGION OF INTEREST RECONSTRUCTION OF COMPUTED TOMOGRAPHY IMAGES.

By

MARCO ANTONIO BARRERA CRUZ, B.P.

THESIS

Presented to the Faculty of the Graduate School of

The University of Texas at El Paso

in Partial Fulfillment

of the Requirements

for the Degree of

MASTER OF SCIENCE

Department of Physics

THE UNIVERSITY OF TEXAS AT EL PASO

August 2009

ACKNOWLEDGEMENTS

I want to say thank you to all my honorable committee for their wise contributions to this work.

For Dr. Marian Manciu, I appreciate all the patience and the freedom that he gave me to develop this project from scratch. Also, for all the economic support and all the corridor talks about any subject that helped me in every step of my academic life.

For Dr. Eric Hagedorn, I want to say thank you because you helped me beyond my academic life.

To my friends, because you always encourage me to keep going.

To Dr. Murat Durandurdu, Because after bad days in the classroom he had faith for my academic success.

To Dr. Jorge Lopez, who helped me to get into this Master Program.

To every professor, classmate and the physics department staff who contribute in this work even when they did not know.

ABSTRACT

Computed tomography is one of the most rapidly advancing method in modern medical imaging, because of is relatively low cost and outstanding quality. The main shortcoming of the method is the relatively high dose of radiation used. Consequently, considerable efforts have been made to obtain good image reconstructions from fewer projections or from using lower intensity beams (hence, noisier data). It has been known for decades that a scan with high intensity beams and large number of projections (typically, 180-360 for a planar image) will lead to a very good image reconstruction via an Inverse Radon Transform (IRT), but the method is not accurate when less than 30 projections are employed. On the other hand, algebraic methods are very efficient for small images; unfortunately, for an N x N image, the number of coefficients of the matrix corresponding to the linear system of equations is of the order of N^4. Hence, even for a relatively small images with N=256, the matrix have around 4 billion coefficients. For almost all practical applications of the computed tomography, algebraic reconstruction are prohibitively time consuming.

The aim of this novel method is to combine the advantages of both IRT and ART to obtain a good image for a small region of the total image. Starting with the total projections of the large image, a Filtered Back Projections (FBP) algorithm is used to create an intermediate image; a small Region of Interest (ROI) is selected from the large image and the partial projections belonging to the ROI alone are calculated. These partial projections are subsequently used with an algebraic method to reconstruct the ROI. Assuming a region of interest (e.g., any abnormality suspected to be clinically important) is 10 times smaller than the whole image, the speed of the algebraic method is increased by a factor of roughly 10^6 (e.g, about one second

instead of 10 days); even more important, for three dimensional images, the factor is 10^9 (one second instead of 30 years).

Furthermore, for a small ROI, the system of equations to be solved algebraically become overdetermined even for a small number of available projections, while for the total image the system is severely under determined.

The influence of noise and of the reduced number of projections on the quality of the approximate projections of the ROI image is also investigated.

A new parameter δ is introduced and its defined as the difference of signal levels between the real image and the FBP reconstruction. The optimal value of the new parameter could be determined without using the original image. The quality of the reconstruction of the ROI depends on its size, with a better quality for larger sizes. Also, it was found that the method is robust even in the presence of noise.

TABLE OF CONTENTS

LIST OF TABLES

LIST OF FIGURES

INTRODUCTION

The use of the Computed Tomography (CT) has influenced enormously the imaging medicine for diagnostic or therapeutic purposes. The main advantages of Computed Tomography are: the imaging of the cross sectional parts of the anatomy, the differentiation between distinct tissues, and the fact that it is a non surgical invasive technique.

The quality of the CT reconstructed image, a cross sectional slice of the body, has been improved constantly during the four decades since its first introduction. The reconstruction time that was several hours for a small image has been reduced to less than a second for whole-body imaging. Most of those improvements were due to the progress of the electronic and the physical engineering of the CT scan machines and the algorithms for computerized reconstructions.

While initial CT image reconstructions have been performed with algebraic methods, the Inverse Radon Transform (IRT) is almost always preferred now. The reason is that in order to reconstruct a 2D image of N x N pixels, for any realistic value of N (e.g., N>30) the number of variables exceeds largely the number of equations (the total number of available projections) and the system to be solved is prohibitively large, which makes the algebraic inversion methods unpractical. However, for very small images the algebraic methods performed very well and are in general more accurate than IRT. The aim of this work is to study an hybrid method for computerized tomography reconstruction using a mixture between the Algebraic Reconstruction Technique and the Inverse Radon Transform. The basic idea is to perform a fast algorithm reconstruction for the whole (large) image using an IRT method, Filtered Back Projection (FBP) and a high quality local reconstruction with of a much smaller Region of Interest image using a

powerful Algebraic Reconstruction Technique (ART). The implementation of ART is more involved and uses higher computer resources than the FBP; however it performs better for small images when a reduced number of projections are available. The hybrid method takes advantage of the best characteristics of the FBP and ART methods and it will help to improve local diagnostic and cancer treatment in the future.

The first chapter of this work gives a description of the physical, mathematical and image quality backgrounds. The second chapter talks about the computed tomography principles, tomographic acquisition, CT equipment and dosimetry. The third chapter states the mathematical approach for the tomography reconstruction, describing the mathematical acquisition of the tomography data, the FBP reconstruction algorithm and the ART algorithm. Chapter four describes the novel hybrid method and the procedure to implement it. Also, in this chapter is explained the computational set up of the numerical method. The fifth chapter shows the results of the implementation of the hybrid method; a noise correction of this method implementation that improves the reconstruction; and a study of the local image quality in function of the number of projections with noise and with a variation of the local reconstruction dimension. Finally, discusses the results, conclusions and future work proposed for this project.

CHAPTER 1: BACKGROUND PRINCIPLES

1.1 Physical Principles

While light has been present since the beginning of time, it was only in the 1860's when James C. Maxwell did a great synthesis between the electricity, magnetism and their role in explaining the light. After Maxwell's publication, *electromagnetic radiation* was pronounced as the new name of light and it not only referred to visible light but also to an amazingly wide spectrum of electromagnetic waves (*see figure 1.1*).

Although all electromagnetic radiations share common properties (e.g.: all of them can be described by electric and magnetic fields; all of them travel at the same velocity, the speed of light in vacuum c = 300,000 kms^{-1} all of them are carried by photons) each range of energy has quite different characteristics. The names that are given in the spectrum (*figure 1.1.1*) are related to the manner in which radiation is detected or produced; mathematically, those waves are expressed with the same set of equations.

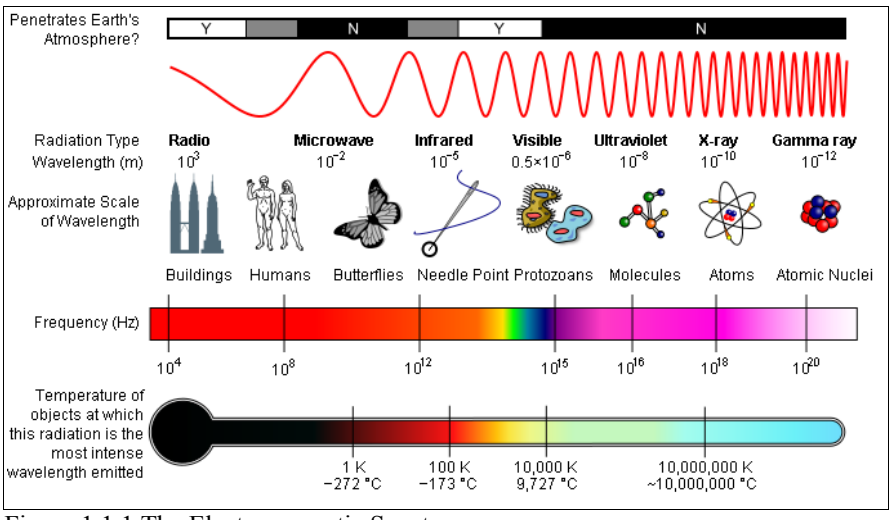

Figure 1.1.1 The Electromagnetic Spectrum.

We will try to explain some of those electromagnetic waves with more detail.

The visible light, is the region more familiar to us because our eyes are adapted to detect a wavelength between 700 nm (red) and 400 nm (violet). Infrared is the light with wavelengths just above of the visible spectrum; and has wavelength between 1 mm to 7 μm and it is associated with thermal energy. Microwaves are considered also short wave radio, this are broad used for communications or radar (and even in the kitchen!). Their wavelength range is from 1 mm to 1 m. The radio wavelength are the most abundant in the universe (background radiation form the big bang) and are generated from different astral bodies while on earth are used for common radio broadcast. Radio wavelengths are those bigger than 1 m. On the other side of the visible spectrum, the ultraviolet light has slighter shorter wavelength (400 nm to 1 nm). X-ray is a energetic radiation that comes from the transition of inner electrons in the atom and from energetic stellar process such as accretion disk around a black hole. The X-ray radiation has wavelength shorter than 1 nm, the soft X-ray with wavelengths of the order of 0.01 nm can easily penetrate the soft tissue but it is stopped by bones and other hard tissues; this is the reason for what is widely used in radiography. Gamma radiation is highly energetic radiation that is produced either by nuclear breakdown or by subatomic particles annihilation.

1.2 X-rays

The use of X-rays are well known, not only for therapy and diagnostic medicine, but also for industrial applications such as the quality control of welding.

Consider an electron with kinetic energy K which is shooting to a molybdenum nuclei target and it is scattered (*see figure 1.2.1*). For that collision, the electron transfers momentum to the atom and it loses kinetic energy (KE). The KE lost by the electron is radiated

for the atom as a X-ray photon with energy $h\nu=\Delta K$. This process is called '*bremsstrahlung*' (German expression for “braking radiation" or "deceleration radiation") and is responsible for the continuous spectrum of the X-ray.

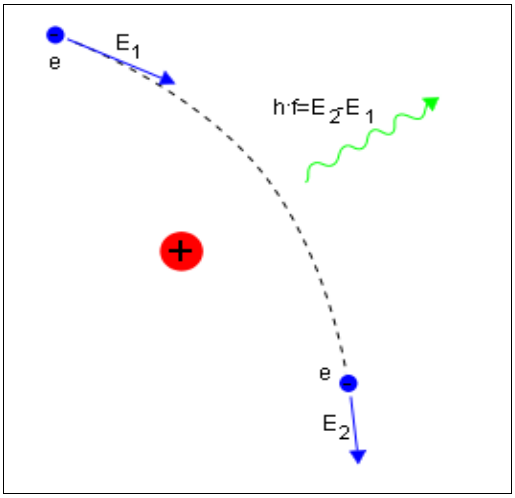

Figure 1.2.1. *Bremsstrahlung* electron effect.

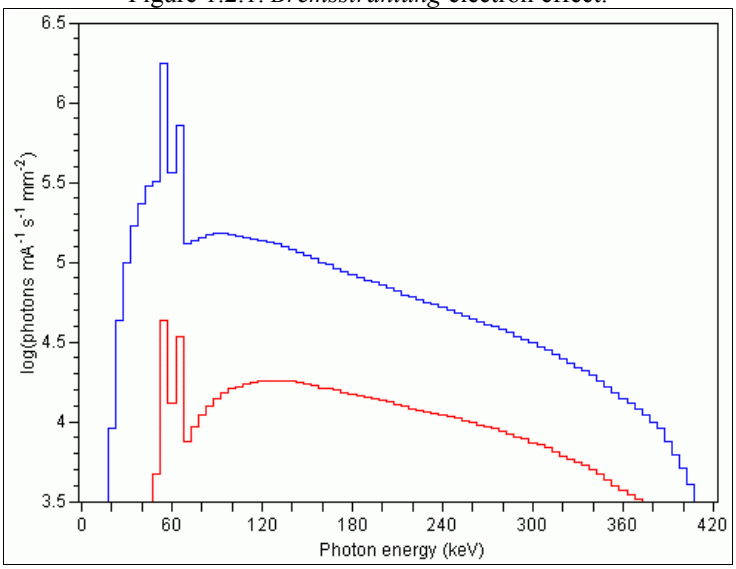

Figure 1.2.2. X-ray continuous spectrum.

Now suppose that the electrons are accelerated by a potential difference V and hit the molybdenum target. Those electrons will lose energy from 0 eV to the K_{max} eV. Therefore those *bremsstrahlung* electrons have a X-ray continuous spectrum from 0 to K_{max}.

One particular characteristic of the continuous spectrum of the *figure 1.2.2* is the existence of a shortest wavelength, λ_{min} (corresponding to the highest energy available to the photon, K_{max}). There are no photons with a shorter wavelength; this is due to the fact that the most energy a photon could get is when the total KE of the electron is lost in one collision, therefore, the atom radiate a single photon with the complete (kinetic) energy of the electron. It is important to say that λ_{min} depends only on the maximum kinetic energy of the electron and not on the target.

From the *figure 1.2.2* , the two peaks K_α and K_β, are called characteristics peaks of a material. When a material is bombarded with electrons and one of those hit the nuclei, it can be able to take off one electron from the inner orbits of the atom. Once the inner orbit of the atom has a vacancy, one outer electron lose energy and goes to fill the inner orbit. If the electron comes from the outer layer *L* (n=2), it will produce the line K_α. If the electron comes from the orbit *M* (n=3), it will radiate the intensity peak for K_β. The intensity of the lines K_α and K_β are related with the difference of energy for the electron in the outer orbit to the inner orbit. Those characteristic lines are different for each element, therefore all the elements might be identified by this method (X-ray spectroscopy).

1.3 Radiation Units

When the directly ionizing radiation such as the x-ray, gamma ray, beta particles, or alpha particles, collide with an atom they can remove an electron from it. This atom without an electron is called a negative ion or ionized atom. Therefore, the radiation is called "Ionizing Radiation". Since the ionizing radiation can damage living tissues of organisms at much smaller dose than the non-ionizing radiation (e.g., visible or radio waves), it has been thoroughly studied for health reasons.

Ionizing radiation can be found in nature as cosmic rays or produced by radioactive elements on the earth, and can be artificially produced by industrial applications or for medicine purposes. We will present a brief description of the radiation units before talking about the radiation dose to living tissue.

The Curie (Ci), is a measurement of the activity or speed of disintegration of a radioactive source. The Curie is defined as :

$$1\ Curie = 3.7\times10^{10}\ \ disintegrations\ \ per\ second\ = 3.7\times10^{10}\ Becquerel\ \ (Bq)$$

The Roentgen (R) measures the radiation exposure, in other words, is the measure of the capacity of a X-ray or Gamma ray beam to ionize a particular substance. Specifically, one Roentgen is defined as the equivalent exposure to produce 1.6 x 10^{12} ion-pairs in one gram of dry air at 1 atmospheric pressure, at sea level, and at room temperature; however it is not directly related to the ionization produced in other materials.

The *rad*, is a measure of real dose delivered to a specific object in terms of transferred energy. *Rad* is an acronym for "Radiation Absorbed Dose". By definition, one object has received *1 rad* when it has absorbed 10^{-5} *J/g* (energy per gram of substance) of ionizing

radiation. For example, one receives about 0.2 *rad* per year from nature or artificial sources; on the other hand, a dose of 300 *rad* is enough to kill a man. It is important to mention that the unit used for the *Rad* in the SI or unit is the *Gray* (Gy) and 1 Gy = 100 rad.

The *rem* is an acronym of *Roentgen Equivalent in a Man* and it is a measure for equivalent dose. It is important to notice that a gamma radiation and neutron radiation can deliver the same amount of energy; but their biological effects are quite different. The rem is calculated by multiply the absorbed dose (rad) and a Quality Factor (QF). For example, for X-ray and electrons the QF = 1, and for neutrons QF = 5. The National Council on Radiation Protection stated that any person cannot be exposed to more than 5 *rem* per year for labor reasons. Also the *rem* has it SI unit equivalence and it is the *Sievert* (Sv), where 1 Sv = 100 *rem*.

1.4 Image Quality

Image Quality is a stand-alone concept regardless of the medical image modality used, and can be divided among three basic concepts: Contrast, Resolution, and Noise.

1.4.1 Image Contrast

Image contrast is defined as the *difference in the image gray scale between adjacent regions of the image*. It can be classified in subject contrast, detector contrast, and display contrast. The contrast-to-noise ratio is finally employed to judge the quality of an image.

The subject contrast is an aspect of the signal prior to be processed or recorded and it is related to the size of a patient, because the thickness' differences lead to a difference in signals. This difference could be defined with the following expression

$$C_s = \frac{A-B}{A} \quad \text{Eq.(1.4.1.1)}$$

where

$$A = N_0 e^{-\mu x}$$
$$B = N_0 e^{-\mu(x+z)} \quad \text{Eq.(1.4.1.2)}$$

with x the patient thickness and $z = \Delta x$ a thickness difference. Putting together the previous two equation yields

$$C_s = 1 - e^{-\mu z} \quad \text{Eq.(1.4.1.3)}$$

this last expression show the contrast dependence only from the thickness difference z.

Remembering our notion of object contrast being caused by thickness difference in the object, the thick region of the body, "x" , does not appear in the equation above. Only the thickness difference, z, remains in the equation. When $z = 0$ the $C_s = 0$ and C_s increase as the body's thickness difference increase.

Another important result of the equation 1.4.1.3 is its dependence on the attenuation coefficient μ. Just like increment of z, μ increase the subject contrast, too.

For example, for x-ray, when the energy is changed from 40 kV to 20 kV, the attenuation coefficient increases by a factor of about three. Therefore, the subject contrast will increase by a factor close to 3. This results shows the dependence of the subject contrast on x-ray energy, plotted in figure 1.4.1.1.

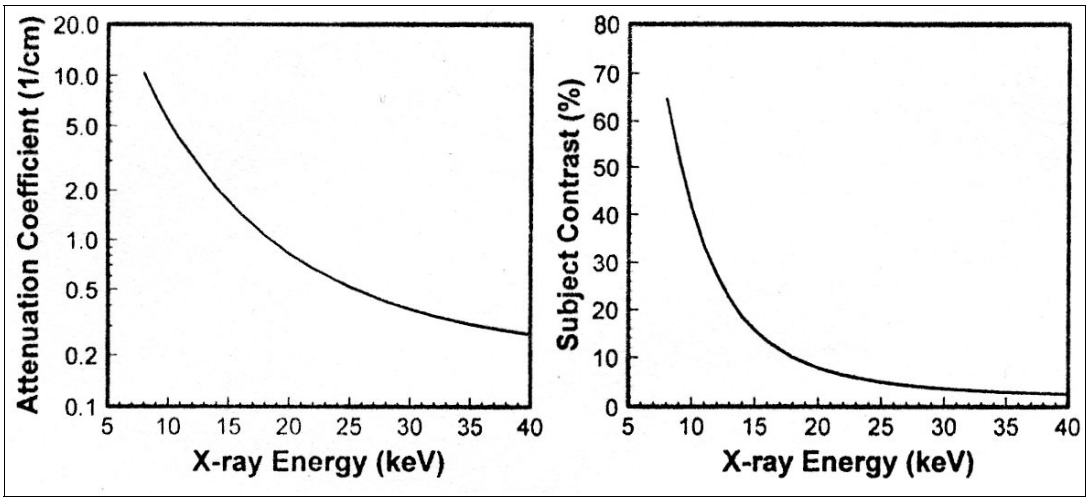

Figure 1.4.1.1. Attenuation coefficient as function of x-ray energy (left) and subject contrast as a function of x-ray energy.

The detector contrast, C_d, is determined primarily by how the detector transforms detected energy into an output signal. Small changes in input energy striking the detector (subject contrast) might result in changes in signal (image contrast). Each detector has a difference of efficiency and because of that, the detectors can amplify unevenly the contrast.

The output of a digital imaging system is a digital image, and the unit that conveys the light and dark properties for each pixel is called a *gray scale value*, or sometimes a *digital number*. Many digital systems have linear characteristic curves while some others have an logarithmic response, such as computed radiography screens and film digitizers.

The detector contrast is the slope of the characteristic curve. For example, for a screen-film system, the exposure axis is usually plotted using a logarithmic scale, and the slope at any point along the curve is called γ:

$$\gamma = \frac{[OD_A - OD_B]}{[\log(A) - \log(B)]} \quad \text{Eq.(1.4.1.4).}$$

The contrast is defined differently for digital imaging system and for screen-film

radiography. The *radiographic contrast* is used for radiography and mammography film based and is defined as:

$$C_R = OD_A - OD_B \quad \text{Eq. (1.4.1.5)}$$

where A and B refer two adjacent regions on the radiography. Radiographic films are placed over light boxes and the contrast cannot be adjusted or enhanced on these analog films.

The digital image contrast (contrast-to-noise ratio) is the post-recorded signal process for which the noise plays an important role. Let *A* and *B* two adjacent regions of the image, and *k* an (off set noise) value of noise in the image. From the equation 1.4.1.1, we will subtract the offset noise *k* yielding

$$C_{s/n} = \frac{(A-k)-(b-k)}{A-k} = \frac{A-B}{A-k} = \frac{A-B}{\sigma} \quad \text{Eq.(1.4.1.6)}$$

where we redefine σ as noise parameter.

Finally, the displayed contrast is a characteristic just for digital images and it is referred to the change of the gray scale (computer assisted) of the image [5].

1.4.2 Image Resolution

There are some misconceptions about the dimension of the image, for example, a 2 dimensional image really has three dimensions: height, width, and gray scale. The height and width are spacial dimensions, and have units of length. Spatial resolution is a property that describes the ability of an imaging system to accurately depict objects in the two spatial dimensions of the image. The closer together they are, with the image still showing them as separate objects, the better the spatial resolution. At some point, the two objects become so close that they appear as one, and at this point spatial resolution is completely lost.

The spatial domain simply refers to the two spatial dimensions of an image (x-y dimension). The resolution on a detector system is measured in the spatial domain by stimulating the detector input, and recording its response. The image produced from a single point (or pixel for digital image) after the stimulus is called point spread function (PSF). For example, for Computed Tomography, a very thin metal wire is placed perpendicular through the slice to be imaged (see figure 1.4.2.1).

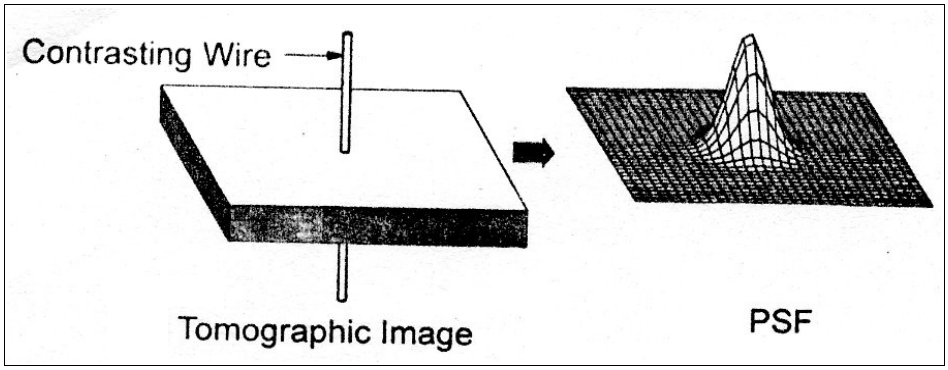

Figure. 1.4.2.1. A point stimulus to a tomographic imaging system can be a long thin wire perpendicular to the tomographic plane (left picture). The PSF resulting the from the wire.

If the PSF is measured at different regions of a detector system and if it is the same for all the region, the imaging system is said to be *stationary*. On the other hand, if the PSF changes from one region to another is said to be *nonstationary* (see figure 1.4.2.2).

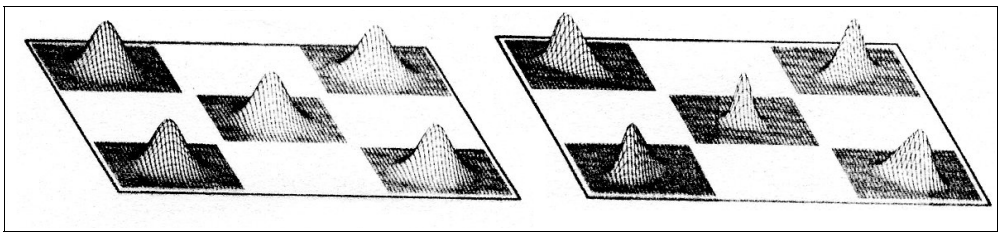

Figure. 1.4.2.2. Stationary PSF (left) and nonstationary PSF (right).

The PSF also describe the blurring from the images, since a images is a set of

different point stimulus, you get back a set of PSF. Also, the inverse process is possible using the Fourier transforms and deconvolution [5].

1.4.3 The Modulation Transfer Function: MTF(f)

Let us imagine a series of sine waves with different spatial frequencies (cycles per unit of length), and let us define the contrast as a difference between its peaks and valleys. Also, the amplitude of each sines waves corresponds to the image density (optical density for film radiography or gray scale for digital image). Each peak of the sine waves will be blurred by the the point spread function of the imaging system, therefore a reduction of the amplitude in their output signal. Note that the PSF will be a greater amplitude (contrast) decrease when the waves have high frequencies. The modulation is essentially the output contrast normalized by the input contrast. The modulation transfer function (MTF) of an imaging system is a plot of the imaging system's modulation against the spacial frequency.

The MTF is a very complete description of the resolution properties of an imaging system. The MTF shows the fraction of an object's contrast as a function of the size of the object or spatial frequency (see figure 1.4.3.1) [5].

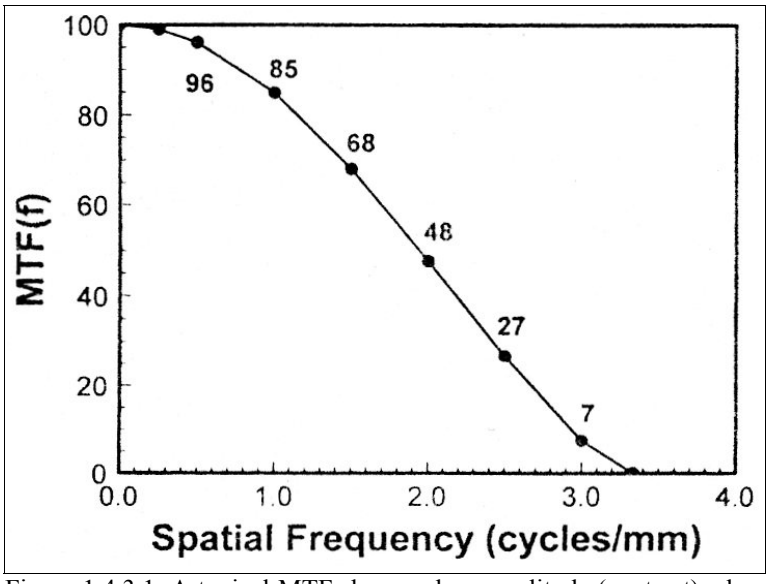

Figure 1.4.3.1. A typical MTF shows a low amplitude (contrast) when the spatial frequency is bigger (object's size is smaller).

1.4.4 Noise

Noise is a positive or negative value added to each recorded signal. And it a general belief that noise values are stochastic, however, there are statistics methods to describe its fluctuations as standard deviations and probabilistic distributions.

Let define the average for n measures as:

$$\mu = \frac{\sum_{i=1}^{n} x_i}{n} \quad \text{Eq. (1.4.4.1)}$$

and the standard deviation:

$$\sigma = \sqrt{\frac{\sum_{i=1}^{n} (\mu - x_i)^2}{n}} \quad \text{Eq. (1.4.4.2)}$$

where x_i is a random variable.

This parameter will describe the characteristics or shape of the Normal Distribution

Statistic Function, also called Gaussian Distribution, as follows:

$$G(x)=\frac{1}{\sigma\sqrt{2\pi}}e^{\frac{-(\mu-x)^2}{2\sigma^2}} \quad \text{Eq. (1.4.4.3)}$$

There is another usual distribution statistic function called Poisson Distribution, that depends only on the parameter μ and is given by

$$P(x)=\frac{\mu^x}{x!}e^{-\mu} \quad \text{Eq.(1.4.4.4)}$$

Both functions are good descriptors of the noise distribution but they have their inconvenience. The Poisson Distribution is useful for small number of measurements. The Gaussian Distribution can be computed more easily, but depends on two variables.

The Gaussian distribution is a good approximation to the Poisson Distribution when the standard deviation is equal to the squared root of the average. As an example, X-ray counting statistics obey the Poisson distribution. For this behavior, σ can be predicted from the average (μ), it imply that the noise (σ) can be adjusted in an image be adjusting the (μ) number of photons used to produce the image [5].

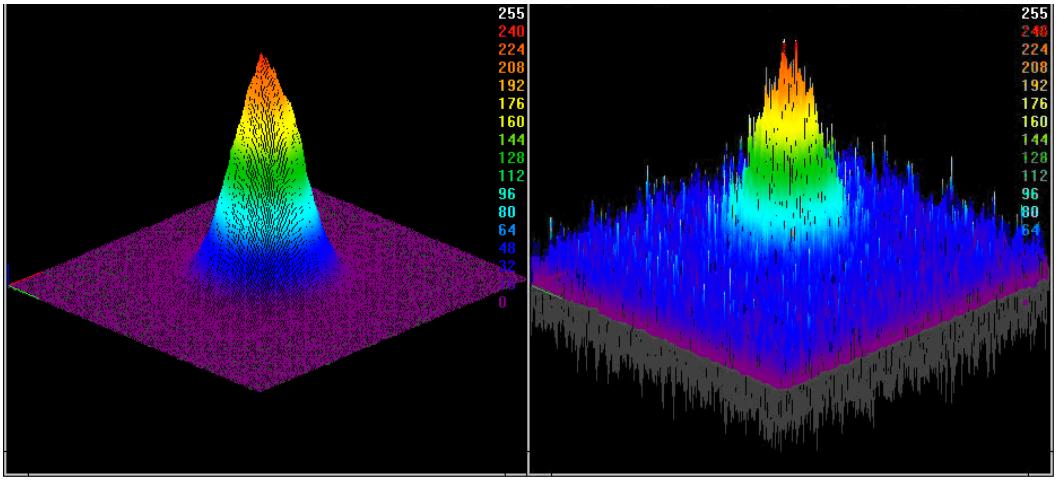

Figure 1.4.4.1 A punctual clear image (left) and the image with high random noise (right).

As an example, in the figure above an image of a punctual object is presented, for negligible and light values of random noise.

1.4.5 Quantum Noise

In the field of medical imaging the term *quanta* is a generic term for a single discrete and packed signal. The term quantum means "*countable"* . In medical imaging the x-rays, electrons, ions, and light photons are example of quanta. For x-ray quanta, it is common to name the number of photon per unit area with the symbol *N*. For digitals x-ray detectors, the recorded average number of photons per pixel is *N* and its related noise is:

$$\sigma = \sqrt{(N)} \quad \text{Eq.(1.4.5.1)}$$

where σ is the *standard deviation* or the noise, and σ^2 is the *variance*. The relative noise or coefficient of variation is defined as:

$$Relative \;\; noise = COV = \frac{\sigma}{N} \quad \text{Eq.(1.4.5.2)}$$

from the equation 1.4.5.1 we can state that when *N* increase σ increase as the square root of *N*, but the COV decrease when *N* increase. The inverse of the relative noise is the signal-to-noise ratio (SNR).

$$SNR = \frac{N}{\sigma} = \frac{N}{\sqrt{(N)}} = \sqrt{(N)} \quad \text{Eq.(1.4.5.3)}$$

This last equation also gives us a measure of the dose: "*when the number of x-ray quanta N is increased, the radiation dose to the patient also* increases"[5].

For all the x-ray imaging modalities, the pursuit is to reduce the patient's dose to minimum levels but always compromising the dose with the SNR. That way it is important to count every x-ray photon that reaches the detector. An ideal x-ray detector absorbs all the

incident photons, and the SNR is simply to the quantum nature of light. For real detectors this is not true, because they absorb only a limited number of photons. The quantum detection efficiency (QDE) is the ratio of the number of incident (absorbed) photons to the number of emitted photons.

$$QDE = \frac{N_{absorbed}}{N_{incident}} \quad \text{Eq.(1.4.5.4)}$$

and the QDE could also be accounted for in the SNR [5].

$$SNR_{reality} = \sqrt{(N_{detected})} = \sqrt{(QDE \ x \ N_{incident})} \quad \text{Eq.(1.4.5.5)}$$

CHAPTER 2: COMPUTED TOMOGRAPHY

In this chapter we present the concepts of medical imaging, the different modalities for X-ray imaging, the principles of Computed Tomography and a basic idea of the equipment involved.

2.1 Computed Tomography

Computed Tomography (CT) is an extremely successful tool for diagnostic medicine, and was the first technique to image the inner human anatomy by different axial slices. The first CT machine was a scanner for head imaging in 1972. This first machine had a poor resolution of 80x80 pixels image with a 3 mm pixel length, the acquisition time was around 4.5 minutes and the reconstruction time of about 1.5 minutes. These poor features of the scanner were practical for the head because of the long acquisition signal time. In contrast, the chest scan requires short signal acquisition times because of the movement due to the respiration and the heart beat.

The implementation of the CT scan by Godfrey Hounsfield and Allan Comark was rewarded by the Nobel Prize for Medicine in 1979. The fast development of acquisition technologies, computer speed, geometry of acquisition, and X-ray tubes have been leading to drastic improvements in CT imaging in the last decades [5].

2.1.1 Basic principles

In 1917 Radon create the first mathematical principles for CT reconstruction. He stated that it is possible to reconstruct an image of an object from a large enough number of projection through it.

Lets suppose that we know *a priori* about the pathology on the chest of a patient, so we will take an X-ray plate with a posteroanterior (PA) projection; this will give us the localization of the pathology on the area of the chest, but it will not give us information about the depth of it. Then, we will take another radiography from the lateral side of the patient. Therefore, with the two images we will have an idea of the depth and localization of the pathology. Now, let us think that we can take 360 X-ray plates with a separation of 1^{o} degree around the anatomy of the patient. These 360 images will give us the inner image or cross sectional image of the patient's body, however, it will be impossible for a human to visualize this image. On the other hand, a computer can store all this information and, by using a reconstruction numerical method, can display a two dimensional image of the patient's inner body.

2.1.2 Tomographic Acquisition

In order to understand the signal acquisition for a tomographic reconstruction, we have to define some basic vocabulary. For a single transmission measurement through a body from an emitter to a single detector is called *ray*. A series of rays that pass through a body with the same orientation is called a *projection*. There are two types of projections; among the simplest ones are the parallel beam (PB) and the fan beam (FB). The PB as its name says is a set of rays parallel to each other, on the other hand in the FB all the rays diverge from the source

point and the geometry looks like a fan. The FB geometry is used for modern CT scan machines. One single axial image could have up to 800 000 transmission measurements. After the first image, the CT scan machine move the patient on the z-axis, perpendicular to the cross sectional area, to produce the next slice or image of the inner body of the patient.

2.1.3 Tomographic Reconstruction

For each X-ray emitted exist an associate detector that measures an attenuated intensity I_a and the unattenuated intensity I_0 is measured by a reference detector at the same time too. The relation between both intensities are associated by the following expression

$$I_a = I_0 e^{-\mu t} \quad \text{Eq.(2.1.3.1)}$$

where μ is the average attenuation function and t is the length along the ray that travels through the patient. It is important to note that Ia and Io are dependent variables given for the scan machine, and μ is the independent variable related with the inner anatomy of the patient. We can solve the last expression for μt to get

$$\ln\left(\frac{I_0}{I_a}\right) = \mu t \quad \text{Eq.(2.1.3.2)}$$

As we mentioned above the Filtered Back Projection is the most used reconstruction technique; it is reviewed in chapter 3.

2.2 CT Equipment

The first CT scan machine, EMI Mark 1, was introduced in 1972 for the head scan. After this first generation machine, several more generations of CT scanners were built. A brief review follows.

The first generation used a scan geometry of PB with a single X-ray emitter and a single X-ray detector. This particular detector used is called Pencil Beam Geometry and was the most accurate for X-ray detection, because it did not measure the X-ray scattered or deflected by the patient's body. However, this detector suffers from “afterglow” noise, that is the remaining signal from the previous reading (if it was close in time). This first generation CT scanner used a Translate-Rotate configuration, which means that the emitter-detector moves first in one axis direction (translating on the axis) and when it ends the first projection, it rotates one degree initializing again the translation on the new axis. This first CT scan used 160 parallel rays and 180 projections with 1 degree interval. The total ray signal acquired was of 28,800 to produce a image of 80 x 80 pixels.

The second generation of CT scan changed drastically the ray signal acquisition and the scan geometry. This second generation used the same Translate-Rotation configuration but used a FB projection geometry. For this geometry, a 10 degrees fan wide range and a linear array of 30 detectors were implemented. The number of ray signal acquisition increased to 324,000 from 600 rays and 540 projections. This second generation was 15 times faster than the first generation but it received more noise from the radiation scattered and deflected by the patient's anatomy.

For the Third generation the translation configuration was removed by making the

fan beam angle sufficiently wide to cover the entire patient's body. This new configuration is called Rotate-Rotate, because both the emitter and detectors rotate at the same time without a translation. This allowed one slice sampling in about 5 seconds. On the other hand, because of the high number of detectors used and the electronic associated with them, the cost increased drastically in this third generation. Also, in this generation, another problem developed, the *ring artifact* due to the possible existence of a single bad detector that could alter the signal and hence the image reconstruction.

The fourth generation was built to correct the *ring artifact* of the 3th generation; essentially represents the same machine, but with the detector array changed to a 360 stationary array of detectors. In fact, the 4th generation CT scan machines uses 4,800 detectors in a circular array around the patient. It means that this 4th generation has an Rotational-Stationary configuration but with a fan detector geometry and that the X-ray emitter rotates in a fan geometry with focus in each detector once at the time.

The fifth generation was created just for cardiac imaging and was called *electron beam scanner*. This scanner works with a Stationary-Stationary configuration. Also it does not use the conventional X-ray tubes, instead, uses a tungsten rings all around the patient that are struck by an electronic cone beam. This scanner can get cardiac images at 0.05 seconds intervals.

The sixth generation use the third and fourth configuration with the addition of *slip rings* instead of wires for the rotational instruments. These slip rings are made with wired brushes that can travel free on a ring giving the signal along the 360 degrees. This new technology allows the *Helical Scan* by the continuous rotation of the X-ray and the translation of the patient table perpendicularly to the center of rotation. This new configuration made the

acquisition time faster.

The last generation, the seventh, uses the technology of the 4th and 6th generation and adds a 2 dimensional detector array that allows an increased X-ray beam to be scanned at the same time over several slices thicknesses to produce different resolutions images. This generation does not use the Helical Scan technology [5].

The CT equipment has been improving constantly due to better detectors, different geometries, X-ray production tubes, mathematical methods and computational implementation. But there are still compromises between the image quality and the radiation absorbed by the patient, which increase the health risks associated with ionizing radiation. This issue will be addressed in the next section.

2.3 CT Dosimetry

X-ray imaging modalities have different modes to account for the radiation dose delivered to a patient. For example, radiography uses the *exposure entrance* instead of the adsorbed dose. For the CT modality there are three major dose characteristics. First, the body's portion radiated by the beam is smaller than the one irradiated in a radiography; the radiation is more evenly distributed to all patient's body due to the CT geometry of acquisition; and for CT dose radiation is up to 100 times higher than radiography.

Compton effect is the principal scatter interaction between X-rays and matter at typical X-ray energies used in CT. The Compton effect is a change of photon's wavelength (energy) due to an inelastic scattering process on free electrons. A CT scan delivers a primary beam through a slice, but this slice will receive not only a dose from this beam but also from

scattered radiation from contiguous slices. This scattered radiation could be greater than the radiation from the primary beam with an increment of the number of slices scanned.

The Multiple Scan Average Dose (MSAD) is the standard measurement from a CT scan. The MSAD measures the dose not only from the primary beam and its scattering but also from all the scattered radiation from all the CT slices. MSAD is measured by placing a small exposure meter in a phantom at certain depth from the surface between the CT slices and then adding the multiple CT dose. Another way to measure the MSAD is doing a single CT and measure the *CT Dose Index* (CTDI). The CTDI is defined by the U.S. Food and Drug Agency as " *the radiation dose to any point in the patient including the scattered radiation contribution from 7 CT slices in both direction, for a total of 14 slices* ". This is referred as the $CTDI_{FDA}$. The $CTDI_{FDA}$ is calculated by a single CT scan on a Lucite Phantom, placing ThermoLuminescent Detectors (TLDs) at 14 slice thickness along the phantom, with a single scan at one TLD and adding the readings of the rest of the TLD the $CTDI_{FDA}$ is calculated.

Another common way to measure the CTDI is using a 100 mm ionizing chamber rod. This pen is large enough to cover 14 slices of 7 mm or 8 mm. A single CT image is taken at the middle of the pen, therefore, the CTDI is determined from the reading of this pen. This method cannot be used for the $CTDI_{FDA}$ other than 7 mm slices. However, this method is referred as $CTDI_{100}$ for any slice thickness. It is worth to note that the $CTDI_{100}$ gives a better measures of the MSAD for small slice thicknesses (~ 2mm) than the $CTDI_{FDA}$.

Two kind of phantoms are used to determinate the CTDI a 16 cm diameter head phantom and a 32 cm diameter body phantom. Holes are drilled perpendicular to the diameter of the cylinder shape phantom in order to insert the 100 mm ionizing chambers. The free holes are

filled with Lucite rods and for standard measures of the MSAD the ionizing chambers are positioned at 1 cm from the surface of the phantom and at its center. The medical physicist measures the *Kerma Air*, which is subsequently converted to dose. The CTDI and MSAD are expressed as a Lucite dose. It is important to mention that the dose in CT is directly proportional to the mAs used in each slice. At constant kV, doubling the mAs results in dose doubling. The following table shows some CTDIs [5].

Table 2.3.1. Typical $CTDI_{100}$, manufacturer data.

Peak Kilovoltge (kVp)	**Head phantom (16 cm) mGy**	**Body phantom (32 cm) mGy**
80	6.4	1.5
100	12.3	3.5
120	17.1	6.4
140	23.4	7.2

CHAPTER 3: MATHEMATICAL FRAMEWORK OF TOMOGRAPHY

3.1 Line Integrals and Projections

A line integral is a mathematical operator that runs over a single or multidimensional function over a single o multidimensional line and in a general form can be represented as follow:

$$\int_{\gamma} \vec{F} \cdot d\vec{x}, \quad with \quad \gamma \in R^n \quad \text{Eq. (3.1.1)}$$

In physics a line integral can represent several properties of a phenomena, the most common use is to calculate the work done for a particle or body through a potential φ over a particular path *S*.

$$W = -\int_{\gamma} -\vec{\nabla}\phi \cdot d\vec{s} \quad \text{Eq. (3.1.2)}$$

From the point of view of tomographic research, particularly X-ray tomography, the line integral will represent the signal acquired from an X-ray source through a detector. Let us define a 2 dimensional body such as a non homogeneous function *f(x,y)* on the plane xy. Let us also define the ray path by the parameters *(θ,t)* as follow:

$$t = x\cos(\theta) + y\sin(\theta) \quad \text{Eq. (3.1.3)}$$

Let as also write the relation between the removed part of the X-ray intensity I and the attenuation function *f(x,y)* as:

$$dI = -f(x, y)Idt \quad \text{Eq. (3.1.4)}$$

Here *dI* represents the differential change in X-Ray intensity along the t-direction and *f(x,y)* in the body or attenuation function, then:

$$\int \frac{dI}{I} = -\int f(x,y)\,dt$$

$$p_\theta = -\ln \frac{I}{I_0} = \int_{(\theta,t)line} f(x,y)\,dt \qquad \text{Eq.(3.1.5)}$$

$$p_\theta = -\ln \frac{I}{I_0} = \int_{-\infty}^{\infty}\int_{-\infty}^{\infty} f(x,y)\,\delta(x\cos(\theta)+y\sin(\theta)-t')\,dxdy \quad \text{Eq. (3.1.6)}$$

The equation 5 is known as the *Radon Transform* of the function *f(x,y)*. The simplest projection is a collection of parallel ray integrals as given $p_\theta(t)$ for a constant θ and is known as parallel projection (*see figure 3.1.1*).

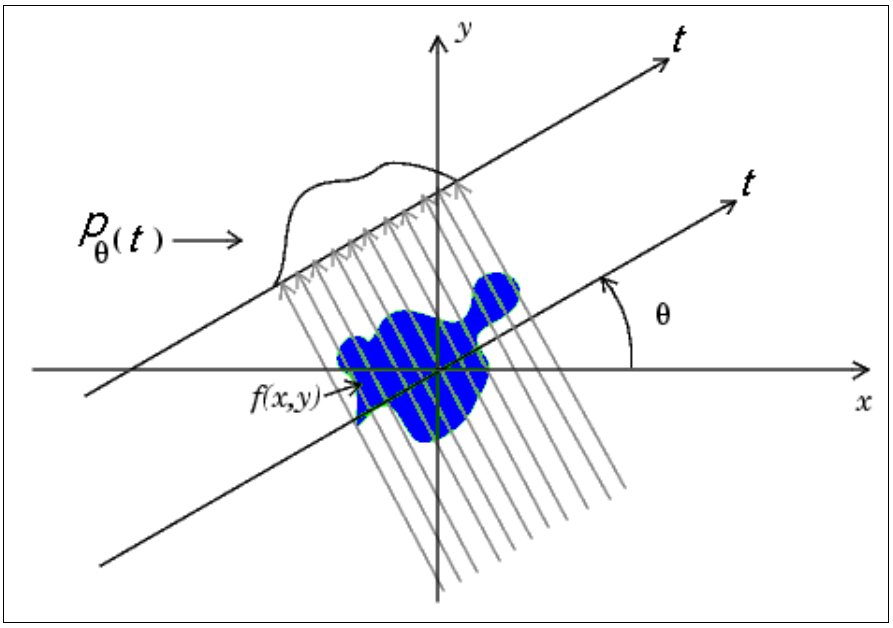

Figure 3.1.1. Parallel projections of a attenuation function *f(x,y)*.

For the discrete case, the equation 3.1.6 becomes a double summation over a discrete matrix function used to calculate the *Radon Transform*.

$$p_\theta = \sum_{-\infty}^{\infty}\sum_{-\infty}^{\infty} F_{ij}\,\delta(x_k\cos(\theta)+y_k\sin(\theta)-t')\,\Delta x\,\Delta y \quad \text{Eq. (3.1.6)}$$

Where $F = a_{ij}$ with dimension $k(\Delta x)\ x\ k(\Delta y)$. Note that when t reaches the coordinates of a_{ij}, the value will be equal to a_{ij}, therefore, the summation over the line t will be equal to the

values of every element a_{ij} that touch the line t (*see figure 3.1.2*).

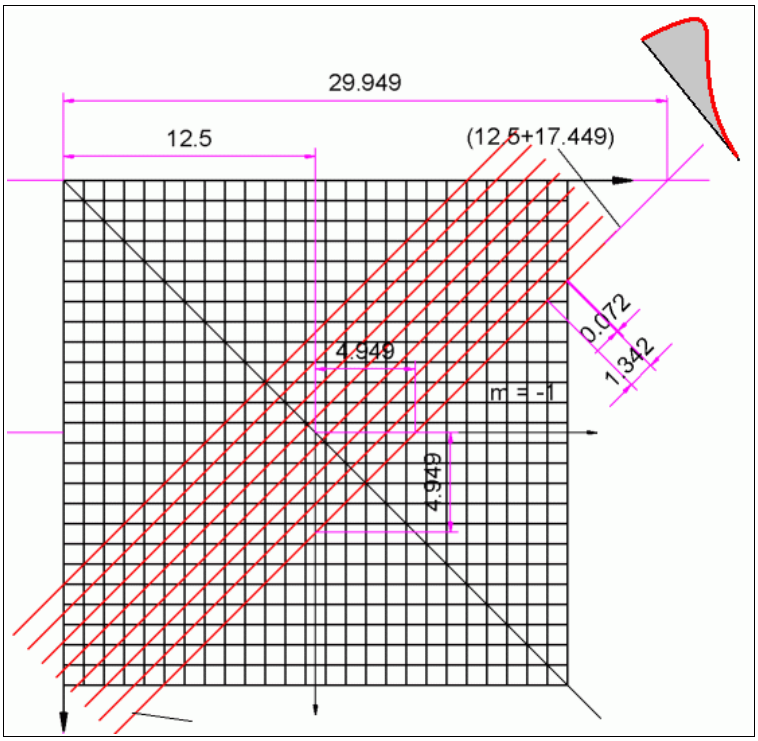

Figure 3.1.2. Summation of the proportional values that cross the line t and the element a_{ij}.

On the other hand, the ART method will use another parametrization to get the projections. This is a weight function w_{ij} for every pixel that touches the line and it is defined as follows:

$$w_{ij} = \frac{(t_{k+1} - t_k)}{\Delta k^2} \quad \text{Eq. (3.1.7)}$$

where $(t_{k+1} - t_k)$ is the length of the intersection of the line t with the pixel a_{ij} and Δk is the length of the pixel (*see figure 3.1.3*). This equation yields a second *Radon Transform* equation for the ART method [17]. For clarity, the we will name Radon Transform the IRT methods and 'projections' the ART methods.

$$p_\theta = \sum_{-\infty}^{\infty} \sum_{-\infty}^{\infty} (F_{ij} \cdot w_{ij})\, \delta(x_k \cos(\theta) + y_k \sin(\theta) - t')\, \Delta x\, \Delta y \quad \text{Eq. (3.1.8)}$$

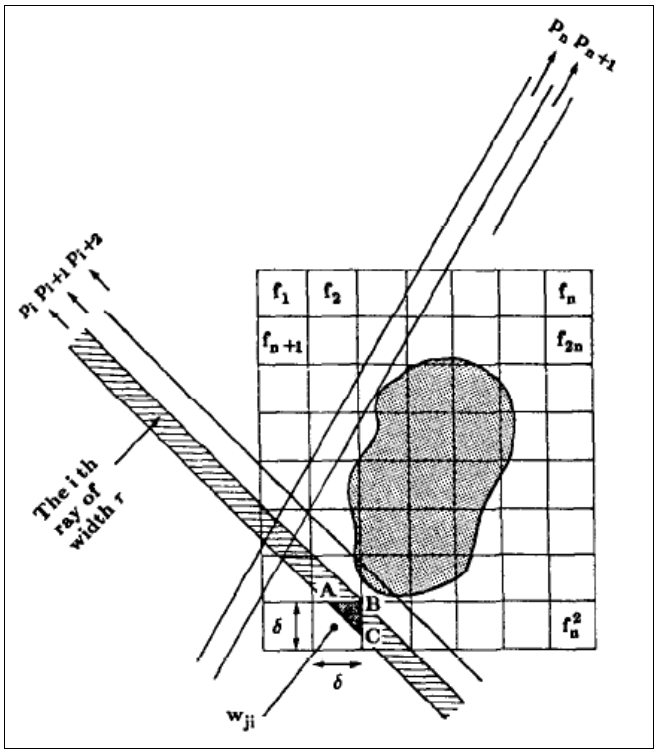

Figure 3.1.3. Radon Transform with weighted cell.

In the next section we will use equation 3.1.7 and 3.1.8 to compute the projections needed for the reconstruction methods IRT and ART.

3.2 Radon Inverse Transform

One of the widely used methods for computerized tomographic reconstructions based on the IRT is the Filtered Back Projected Reconstruction (FBP). The FBP is a simpler and basic IRT reconstruction, which does not yield very good quality images, but it is utilized to as a starting point for other complex algorithms [14]. The FBP will help us to build the hybrid method described on the chapter 4.

3.2.1 Fourier Slice Theorem

The 2D Fourier Transform (FT) was introduced by Bracewell[3] and used by others authors such as Ramachandran and Lakshminarayanan[21]. A detailed description can be found in Kak and Slaney[17]. A *grosso modo* description follows:

The two dimensional Fourier Transform is expressed by:

$$F(u,v)=\int_{-\infty}^{\infty}\int_{-\infty}^{\infty} f(x,y)\mathrm{e}^{-i2\pi(ux+vy)}dxdy \quad \text{Eq. (3.2.1.1)}$$

Where u, v should have units of 1/Length . From the unidimensional definition of the Fourier Transform, it is possible to find the FT of the any projection at any angle. This is:

$$S_\theta(\omega)=\int_{-\infty}^{\infty} P_\theta(t)\mathrm{e}^{-i2\pi\omega t}dt \quad \text{Eq. (3.2.1.2)}$$

now we can define a new coordinates system

$$\begin{pmatrix} t \\ s \end{pmatrix}=\begin{pmatrix} \cos(\theta) & \sin(\theta) \\ -\sin(\theta) & \cos(\theta) \end{pmatrix}\begin{pmatrix} x \\ y \end{pmatrix} \quad \text{Eq. (3.2.1.3)}$$

with this coordinate system a projection will be defined as

$$P_\theta(t)=\int_{-\infty}^{\infty} f(t,s)ds \quad \text{Eq. (3.2.1.4)}$$

plugging equation 3.2.1.4 in 3.2.1.2 yields to the next expression

$$S_\theta(\omega)=\int_{-\infty}^{\infty}\left[\int_{-\infty}^{\infty} f(t,s)ds\,\mathrm{e}^{-i2\pi\omega t}\right]dt \quad \text{Eq. (3.2.1.5)}$$

that at the same time it could be expressed in Cartesian coordinates

$$S_\theta(\omega)=\int_{-\infty}^{\infty}\int_{-\infty}^{\infty} f(x,y)\mathrm{e}^{-i2\pi\omega t}dxdy \quad \text{Eq. (3.2.1.6)}$$

with

$$t = x\cos(\theta) + y\sin(\theta) \quad \text{Eq. (3.2.1.7).}$$

The equation 3.2.1.6 describes the FT of the 2-D density attenuation function with the left side of the equation similar to the 1-D FT of the projections. This equation implies that the 1D FT of the projections of one object, at certain angle θ, is equivalent to the 2-D FT of the density attenuation function along of the n-lines t at certain angle θ. Therefore, for a large number of projections θ, we will have a well sampled attenuation function in the Fourier space, which could be inverted (with a Inverse FT) to reconstruct the attenuated function *f(x,y).* This is,

$$f(x,y) = \int_{-\infty}^{\infty}\int_{-\infty}^{\infty} S_\theta(\omega) e^{i2\pi(ux+vy)} du dv \quad \text{Eq. (3.2.1.8)}$$

which represent the back projection along the line t at given θ. The Fourier Slice Theorem give us a base to use the FT-algorithms in computerized tomography.

3.2.2 Filtered Back Projected Algorithm

The FBP algorithm states that for each angleθ and projection line t, there is a function $Q(\theta,$ t), called the "filtered projection", that contribute homogeneously at every point of t for the function *f(x,y)* previously projected at an angle θ. Mathematically, it can be explained as follows.

The Equation (3.2.1.5) the Fourier Transform could be also rewritten as:

$$S_\theta = F(w\cos\theta, w\sin\theta) = F(u,v) \qquad \text{Eq. (3.2.2.1)}$$

by doing a coordinate transformation:

$$\begin{aligned} u &= w\cos\theta \\ v &= w\sin\theta \end{aligned} \qquad \text{Eq. (3.2.2.2)}$$

and the differential of this transform is

$$dudv = |J(w,\theta)|dw\,d\theta = w\,dw\,d\theta \quad \text{Eq. (3.2.2.3)}$$

with the quantity between the bars is the determinant of the Jacobian. Therefore the equation 3.2.1.7 on polar coordinates yields

$$f(x,y) = \int_0^{2\pi}\int_0^{\infty} F(w,\theta)\,e^{i2\pi w(x\cos\theta + y\sin\theta)} w\,dw\,d\theta \quad \text{Eq. (3.2.2.4)}$$

the outer integral could be expressed as a addition of two integrals one from 0 to π and the other from π to 2π.

$$f(x,y) = \int_0^{\pi}\int_0^{\infty} F(w,\theta)\,e^{i2\pi w(x\cos\theta + y\sin\theta)} w\,dw\,d\theta + \int_{\pi}^{2\pi}\int_0^{\infty} F(w,\theta+\pi)\,e^{i2\pi w(x\cos\theta + y\sin\theta)} w\,dw\,d\theta \quad \text{Eq.(3.2.2.4)}$$

Using the properties of FT for phase and frequency, the Equation 3.2.2.4 can be simplified.

$$F(w,\theta+\pi) = F(-w,\theta) \;\wedge\; |X(-w)| = |X(w)| \quad \text{Eq. (3.2.2.5)}$$

$$f(x,y) = \int_0^{\pi}\left[\int_{-\infty}^{\infty} F(w,\theta)|w|\,e^{i2\pi w(x\cos\theta + y\sin\theta)}\,dw\right]d\theta \quad \text{Eq.(3.2.2.6)}$$

The inner integral in Equation 3.2.2.6 is called a filtering operation, where $|w|$ is the frequency response of the system. Therefore the solution to this inner integral equation is called Filtered Projection and is represented with $Q(\theta)$.

$$Q(\theta) = \int_{-\infty}^{\infty} F(w,\theta)|w|\,e^{i2\pi w(x\cos\theta + y\sin\theta)}\,dw \quad \text{Eq. (3.2.2.7)}$$

therefore Equation 3.2.2.6 becomes:

$$f(x,y)=\int_0^{\pi} Q(\theta)d\theta=\int_0^{\pi} Q(x\cos\theta+y\sin\theta)d\theta \quad \text{Eq.(3.2.2.8)}$$

This last equation is known as the *back projection integral for reconstruction of the function f(x,y)*.

3.2.3 Filter Kernel

From the Equation 3.2.2.6, the inner integral is the representation the Inverse FT of the filter or the Inverse FT of the kernel. There are several types of kernels (also called filters, such as Lak or Hamming).

The convolution or filtration is needed to eliminate the blur data at the edges of the back projected image. But the projected data needs a correction before it is reprojected into the image matrix. If we consider the real image and the reconstructed image, we can notice that one the attenuation of one pixel affect the neighbor pixels of image matrix when it is reconstructed.

Fortunately, this spread of the pixel value can be eliminated.

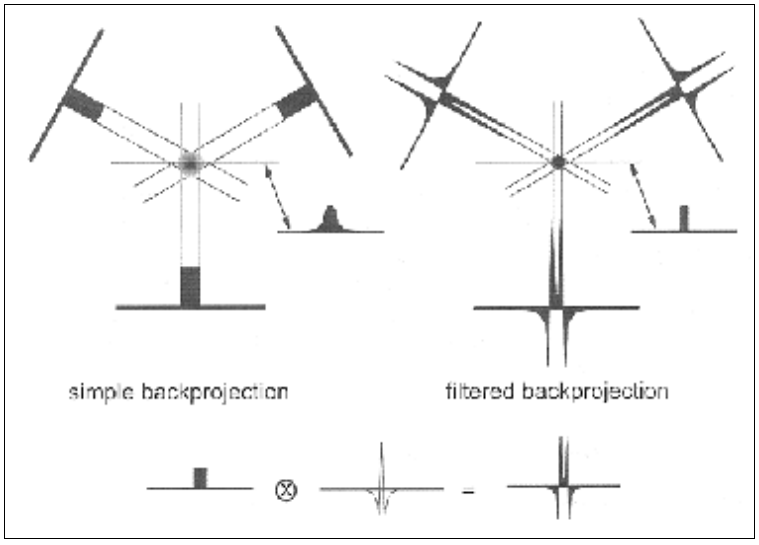

Figure 3.2.3.1. Convolution of the signal with the filter function and re projection.

In this work the Kernel used was the one developed by Waqas Akram[1] :

$$K(\omega)=\frac{8}{a^3\omega^2}\left|\sin(a\frac{\omega}{2})\right|\sin^2(a\frac{\omega}{2}) \quad \text{Eq. (3.2.3.1)}$$

In this Kernel the parameter "a" varies the filter magnitude response, when "a" is very small (a<<1), the response approach |w|. On the other hand, when "a" is big, the filter response starts to roll off at high frequencies.

3.3 Algebraic Reconstruction Technique

The Algebraic Reconstruction Technique is a different approach for tomographic imaging and it forms a large family of methods. The main idea of this method is to assume that the image consists of an array of unknown parameters and to set up a set of algebraic equations for those parameters from the projection data. The system of equation could be, at least in principle, solved and therefor the image can be reconstructed. This idea is simpler than the conceptual approach for the IRT methods.

From the equation (3.1.8), the ray sum at a given at *k-th* angle θ and in a *l-th* ray can be expressed as:

$$\sum_{i=1}^{N}\sum_{j=1}^{N} w_{ijkl}\,a_{ij}=p_{kl}, \quad with \quad l=1,2,3,..,M \ \wedge \ k=\theta \quad \text{Eq.(3.3.1)}$$

Where M is the total number of rays and w_{ij} is the weighting factor for the *ij cell* of the *ij image cell* intercepted by the *lth* ray.

Considering the case of only two variables a_1 and a_2 for the sake of explanation, the following equations would be obtained:

$$w_{11}a_1 + w_{12}a_2 = p_1$$
$$w_{21}a_1 + w_{22}a_2 = p2 \quad \text{Eq. (3.3.2)}$$

From one point of view we can see a_1 and a_2 as a linear base over a vectorial space. A linear combination of the two bases create the vectors p_1 and p_2. Let p_1 and p_2 two non parallel lines on the a_1 x a_2 space and Let $\mathbf{F}^0$ be an initial guess of the vector solution. We initiate projecting $\mathbf{F}^0$ to the first line p_1, and then to the second line p_2. We will re-projecting to each line iteratively, and if a solution exists, the process will converge to an solution in an open set of radius ε, with $\varepsilon > 0$. This is known as The Kaczmarz Method to solve algebraic equation (*see figure 3.3.1*) [17].

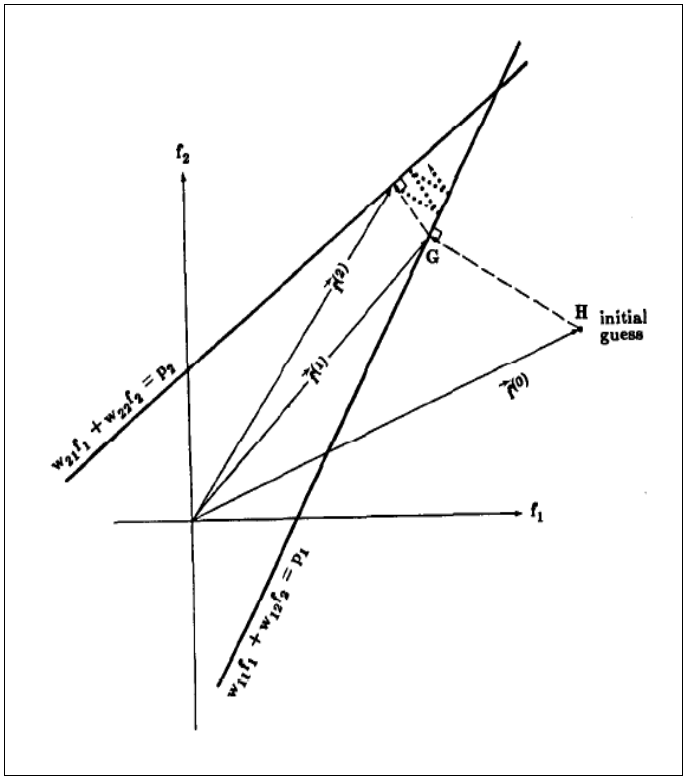

Figure 3.3.1 The Kaczmarz Method to solve algebraic equation.

From the figure 3.3.1, we can defined the quantities:

$$\vec{w}_i=(w_{i1},w_{i2});\quad \vec{f}=(a_1,a_2);\quad for\ i=1$$
$$\rightarrow\ \vec{w}_1\cdot\vec{f}=p_1\ \wedge\hat{w}_1=\frac{\vec{w}_1}{\|\vec{w}_1\|} \qquad \text{Eq.(3.3.3)}$$
$$Also,\ let\ \overline{OU}=\hat{w}_1=\frac{\vec{w}_1}{\|\vec{w}_1\|}$$

We can defined $\overline{OA}$ as the distance from the origin to the plane p_1.

$$\overline{OA}=\vec{OU}\cdot\vec{OC}$$
$$with\ \ \vec{OC}=\vec{f}\ ; \qquad \text{Eq. (3.3.4)}$$

$$\overline{OA}=\frac{1}{\|\vec{w}_1\|}(\vec{w}_1\cdot\vec{f})=\frac{1}{\|\vec{w}_1\|}(p_1)=\frac{p_1}{\|\vec{w}_1\|} \quad \text{Eq. (3.3.5)}$$

To obtain $\mathbf{F}^1$ from $\mathbf{F}^0$ we have to subtract the vector **GH**:

$$F^1=F^0-\vec{GH} \quad \text{Eq. (3.3.6)}$$

$$with\ \ |\vec{GH}|=|\vec{OF}|-|\vec{OA}|$$
$$where\ \ |\vec{OF}|=F^0\cdot\hat{w}_1=\frac{F^0\cdot\vec{w}_1}{\|\vec{w}_1\|} \quad \text{Eq. (3.3.7)}$$

Using equation 3.3.5:
$$|\vec{GH}|=\frac{F^0\cdot\vec{w}_1}{\|\vec{w}_1\|}-\frac{p_1}{\|\vec{w}_1\|}$$
$$|\vec{GH}|=\frac{F^0\cdot\vec{w}_1-p_1}{\|\vec{w}_1\|}$$

$$so,\ \ \vec{GH}\,|\vec{GH}|=\left(\frac{F^0\cdot\vec{w}_1-p_1}{\|\vec{w}_1\|}\right)\vec{w}_1 \quad \text{Eq.(3.3.8)}$$

Note that **GH** is in the same direction of $\boldsymbol{w_1}$. Plugging into equation (3.3.6) yields

$$F^1=F^0-\left(\frac{F^0\cdot\vec{w}_1-p_1}{\|\vec{w}_1\|}\right)\vec{w}_1 \quad \text{Eq. (3.3.9)}$$

Then, for the system of the equations (3.3.2), this will approach the solution. In general, for the system of equations (3.3.2) the recurrent formula will be:

$$F^n = F^{n-1} - \left(\frac{F^0 \cdot \vec{w}_{kl} - p_{kl}}{\|\vec{w}_{kl}\|} \right) \vec{w}_{kl} \quad \text{Eq. (3.3.10)}$$

Note that this equation could be iterated indefinitely thus is:

$$\lim_{n \to \infty} F^n = F_{solution} \quad \text{Eq. (3.3.11)}$$

On the other hand, the equation 3.3.11 is not accurate when the system is over determined (there are more equations than variables). In this case, the intersection of every plane p_{kl} does not occur in a single point, but yields an infinite family of oscillating solutions around the real solution (*see figure 3.3.2*) [17].

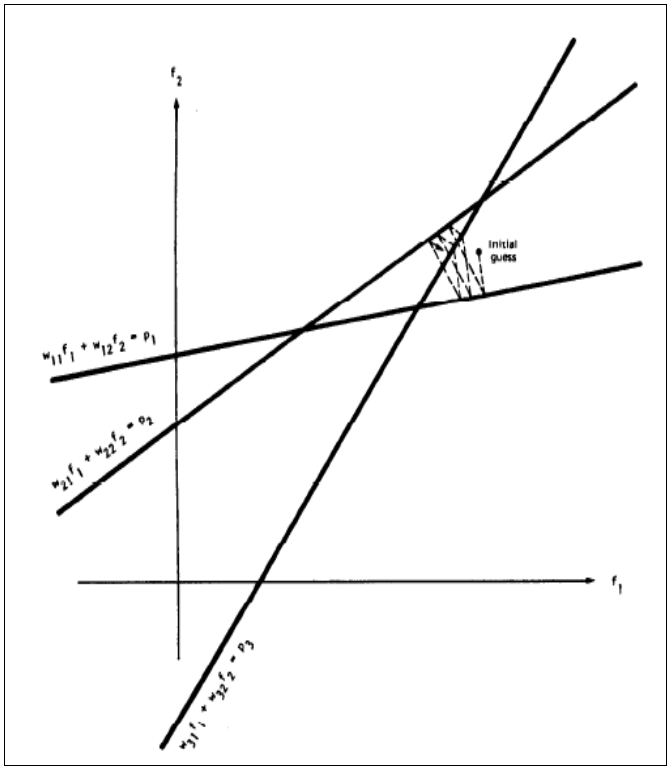

Figure 3.3.2. Oscillatory solution for a linear system of equation with noise.

Despite the noise and the convergence problem, the solution provided by (3.3.11) is in general accurate We implemented computationally this equation to reconstruct the data

acquired by the equation (3.1.8) and the result will be shown in the next chapter.

3.4 Region of Interest

The Region of Interest (ROI) could be defined as a small region in which exists something abnormal to be imaged with more resolution. For Imaging a ROI, it is a sub matrix (sub image) of the original matrix (image). Mathematically it can be stated as:

Let define a matrix I^{nxm} where every element its part of a squared image with dimensions $(n \times m)$, so a ROI is defined as a group of elements of the matrix I^{nxm}, but not an element of a sub vectorial space of I^{nxm}. The matrix ROI has dimensions $(s \times l)$ with s and l less or equal to n and m respectively.

3.5 Local Reconstruction

Local tomography is the aim to reconstruct a $\varepsilon(r,\theta)$ subset of $p(r,\theta)$ for a given $p(r,\theta)$. where $p(r,\theta)$ is the *Radon transform* of one 2-D attenuation function $f(x,y)$. For IRT it was proved that is not locally invertible [17], which means that for a reconstruction of $\varepsilon(r,\theta)$ in a ROI it is necessary to know the projections even far away of the ROI. It was suggested that a set of truncated projections, such as the ones generated by radiation therapy treatment beams, can be used for reconstruction of ROI [2]. One possibility is using Adaptive Local Tomography (ALT) proposed by Guan [11]. It was suggested that a Multi-Level Scheme Algebraic Reconstruction (MLS-ART) outperforms in this case the conventional FBP method, although several projection artifacts are introduced [10,11]. However, it is important to note that the truncate projections are just a Radon transform over a small centered area of the phantom or patient's body, therefore their aim is to reconstruct both ROI and the full image from a subset of information (incomplete

projections, see figure 3.5.1.

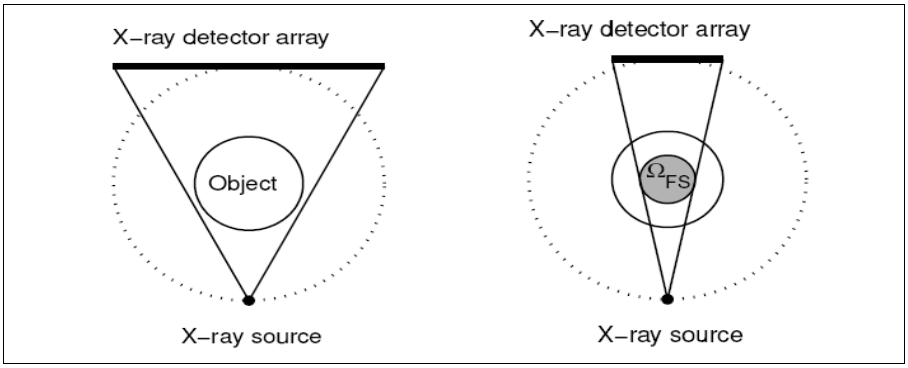

Figure 3.5.1. Representation for standard projections (left draw) and truncate projections (right draw).

In contrast, in this work there is a different aim. We assume that we have a (limited) set of full projections of the image. Using them, of course one can use either FBP or the time-consuming ART to reconstruct the full image. The issue we address is whether it is possible to implement a fast algorithm which can improve ***locally*** the quality of the image, even at the expense of deteriorating the quality of the rest of the image, which is not of interest. In order to do that, we will use FBP to create a rough image, select the region of interest and calculate the approximate partial projections corresponding to the ROI alone. The details of the novel hybrid methods are discussed in the next chapter.

CHAPTER 4: HYBRID METHOD

4.1 Hybrid Method: Algebraic Reconstruction Technique - Inverse Radon Transform.

A novel method that aims at a better reconstruction of the ROI is presented. This method uses as firstly the FBP to reconstruct a full image of poorer quality; the ROI is selected and the approximate partial projections of the ROI are calculated. The latter are used with an algebraic algorithm to create a ROI image of improved quality.

Let P_o the original phantom and the projection is defined as:

$$P_o = a_{ij} \quad , \quad R_o = Radon(P_o, \theta) \quad \text{Eq. (4.1.1)}$$

and the reconstructed image is

$$I_o = FBP(R_o, \Delta\theta) \quad \text{Eq. (4.1.2)}$$

Lets define the ROI interest as follows

$$ROI = [(x_{min}, x_{max}) \times (y_{min}, y_{max})] \quad \text{Eq.(4.1.3)}$$
$$with, \quad ROI \in I_o$$

now we can define two sets:

$$I^c_{o\,ROI} = \begin{Bmatrix} I_o & if & i, j \in ROI \\ 0 & if & i, j \notin ROI \end{Bmatrix} \quad \text{Eq.(4.1.4)}$$

$$I_{o\,ROI} = \{ I_o \;\; if \;\; i, j \in ROI \} \quad \text{Eq.(4.1.5)}$$
$$with, \;\; i = \overline{1 \ldots s} \;\; \wedge \;\; j = \overline{1 \ldots l}$$

note that the dimension of the complement of the *ROI* reconstructed image is the same as the reconstructed image I_o and the *ROI* of I_o dimension is *sxl*.

Applying the Radon Transform to the subset given by the equation (4.1.4) will yield

a projected signal without the *ROI* for the approximate image I_o.

$$R^c_{o\ ROI} = Radon(I^c_{o\ ROI}, \theta) \quad \text{Eq. (4.1.6)}$$

This signal will help us isolate the *ROI* signal from the initial projection, R_o, by a simple subtraction of signals,

$$R_{o\ ROI} = R_o - R^c_{o\ ROI} \quad \text{Eq. (4.1.7)}$$

therefore, the algebraic system of the equation for the ROI will be

$$A\,X = R^c_{o\ ROI} \quad \text{Eq. (4.1.8)}$$

leading to the matrix A to be inverted with the algebraic reconstruction technique presented in the previous chapter.

$$(\boldsymbol{F}\,A)\,X = \boldsymbol{F}\,R^c_{o\ ROI} \quad with \quad \boldsymbol{F} = A^{-1}$$
$$\boldsymbol{F} \approx F^n = F^{n-1} - \left(\frac{F^0 \cdot \vec{w}_{kl} - p_{kl}}{||\vec{w}_{kl}||} \right) \vec{w}_{kl} \quad \text{Eq. (4.1.9)}$$

This procedure can be visualized in the flow chart in the figure (4.1.1).

The method is presented in this section without any algorithms to reduce the noise induced by the Inverse Radon Transform- Radon Transform sequence. Modalities to reduce this noise are analyzed in Chapter 5.

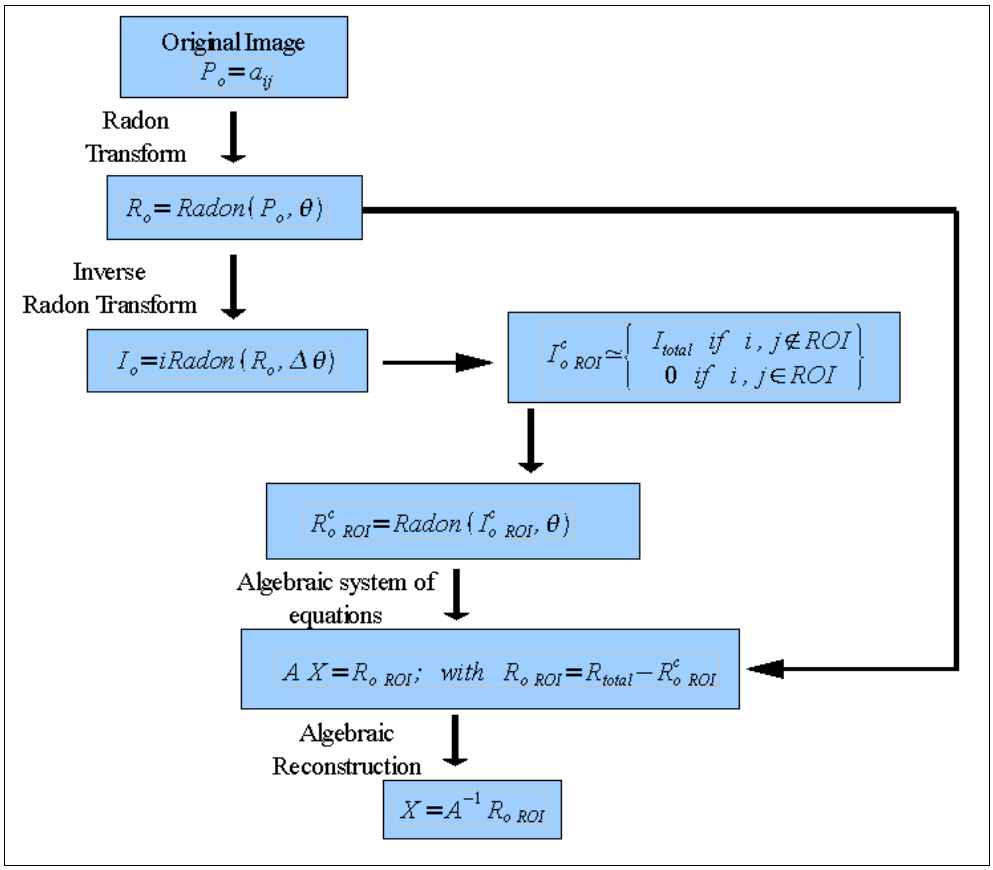

Figure 4.1.1. IRT -ART Hybrid Method flow chart.

4.2 Computational Set Up

The computational Set-Up for the implementation of the IRT-ART Hybrid Method was performed with the software MatLab® R2006a on a generic CPU with a processor Intel® Pentium® Dual CPU E2200 @ 2.20GHz and 4.0 of RAM.

As a vessel Image for tomography, we used the well known '*Shepp-Logan phantom* ' of MathWork, Inc.[23]. The image dimension was fixed at 64 by 64 pixels (*see figure 4.2.1*).

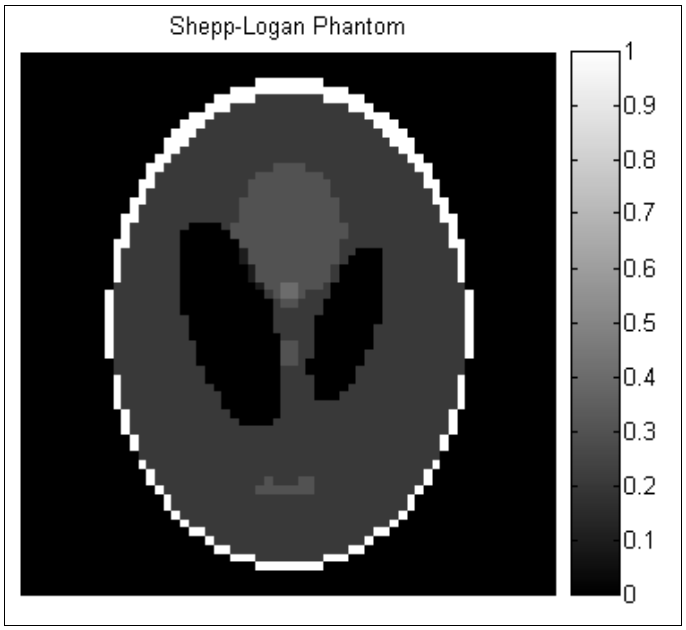

Figure 4.2.1. 64 by 64 Image (Shepp-Logan Phantom) for Tomography.

The projection (equation 3.1.8) series was performed from 1^o to 180^o degrees with 90 ($\sqrt{2}*64\approx90$) rays evenly distributed on a line with a length of $\sqrt{2}$. This is because at 45^o degree projection, the image diagonal image has a length of ($\sqrt{2}*64$) and we consider at least one ray per pixel on the diagonal. Note that in the equation 3.1.8 the pixel weight (triangle) could be seen proportional to the length where a ray cross in the pixel with a value from 0 to $\sqrt{2}*\Delta x$. Where Δx is the length of the pixel.

The FBP (equation 3.3.10) and the ART (equation 3.2.2.8) algorithm were implemented showing a CT test reconstruction in the figure 4.2.2.

Figure 4.2.2. CT reconstruction for 180 projection (q = 1º:1º:180º degrees) and 90 rays evenly spaced over a line (array) of generic length of √2 for a phantom image of 64 by 64 pixels. FBP algorithm shown on the left side and ART algorithm (with 20 iterations) shown on the right side.

We will use the distance function and the correlation coefficient [23] to compute the error of the reconstructed images presented in the following equations:

$$RMS = \left[\frac{1}{N} \sum_{i=1}^{N} (\mu_i - \mu'_i)^2 \right]^{(1/2)} \quad \text{Eq. (4.2.1)}$$

$$CC = \frac{\sum_{i=1}^{N} (\mu_i - \bar{\mu}_i) \cdot \sum_{i=1}^{N} (\mu'_i - \bar{\mu}'_i)}{\left[\sum_{i=1}^{N} (\mu_i - \bar{\mu}_i)^2 \cdot \sum_{i=1}^{N} (\mu'_i - \bar{\mu}'_i)^2 \right]^{(1/2)}} \quad \text{Eq. (4.2.2)}$$

$$\bar{\mu} = \frac{1}{N} \sum_{i=1}^{N} \mu_i \quad \wedge \quad \bar{\mu}' = \frac{1}{N} \sum_{i=1}^{N} \mu'_i \quad \text{Eq. (4.2.3)}$$

where μ_i represent the pixel of the original image and μ'_i the pixel of the second image (a reconstructed i. Also, μ_i and μ'_i *bar* represent the average pixel value (equation 4.2.3).

4.3 Local Image Reconstruction

The original image is presented in the figure 4.3.1 and its 180 projections in a sinogram as a result of the Radon transform (Eq. 3.1.8)

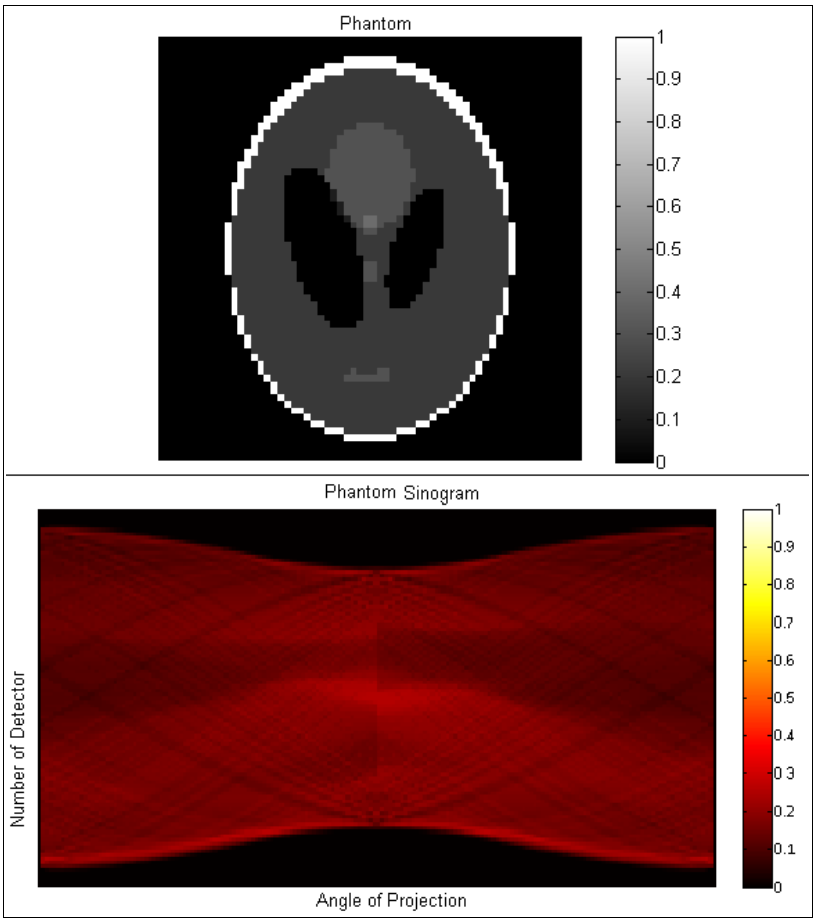

Figure 4.3.1. Original Image 64 by 64 (above) and its projection represented in a sinogram (below) 90 rays and 180 projections from 0º to 180º.

After the Radon transform was performed, the IRT or FBP (Eq. 3.2.2.8) was used to get the reconstructed image, shown in figure 4.3.2.

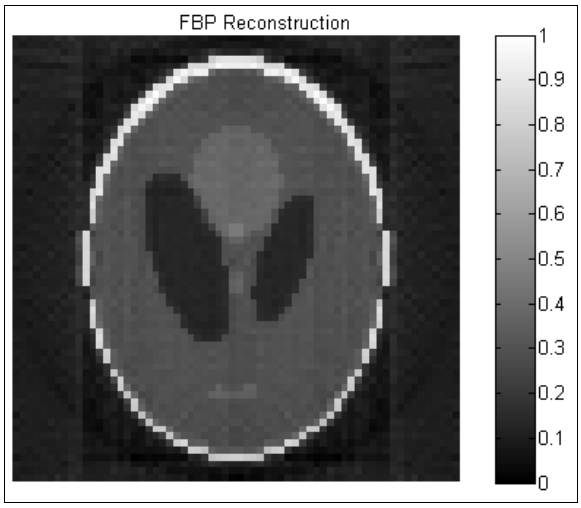

Figure 4.3.2. FBP reconstruction.

In order to judge the quality of the FPB reconstruction, a plot of the pixel values along the same line in both images is presented in the figure 4.3.3.

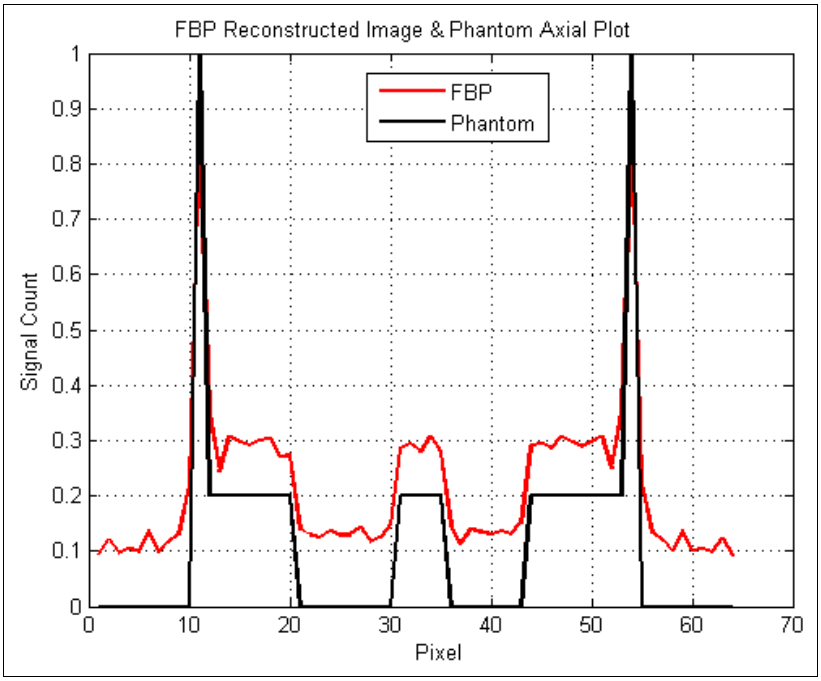

Figure 4.3.3. Pixel values of the row 32 of the reconstructed (red) and original image (black).

The next step is to draw the ROI for the FBP reconstructed image and get the complement image for the ROI (see figure 4.3.4).

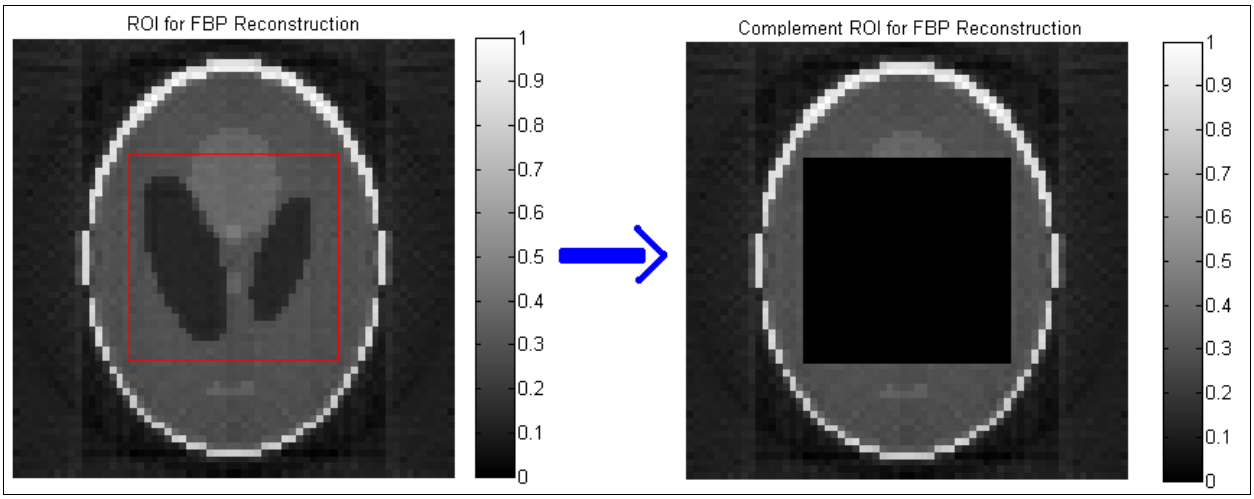

Figure 4.3.4. Region of Interest (size of 30 by 30 pixels) for the FBP reconstructed image (red square, left image) and complement of ROI (right image).

Once the complement of the ROI is defined, this image is reprojected with the Radon Transform (see figure 4.3.5).

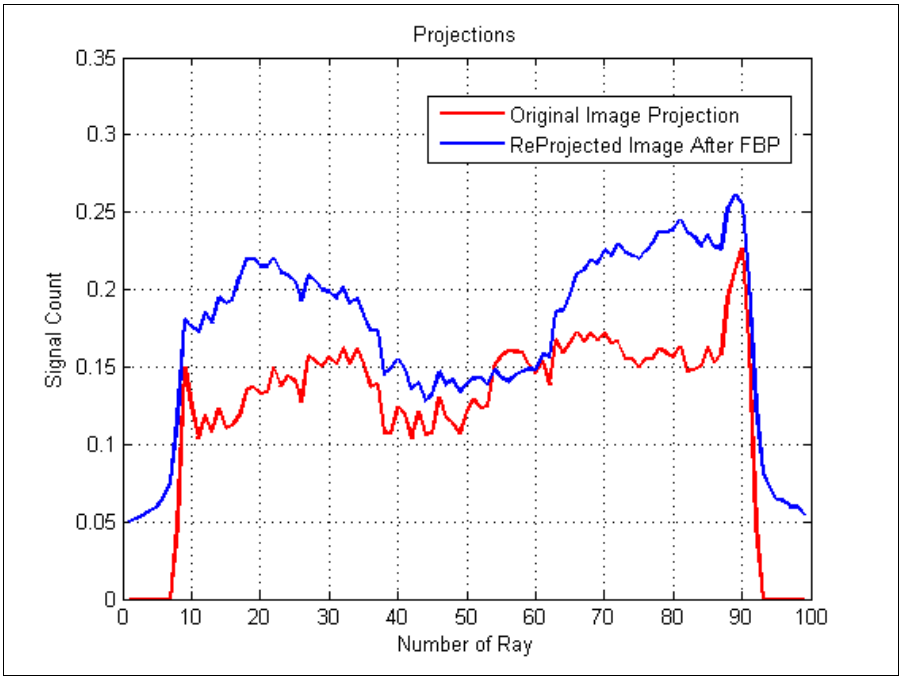

Figure 4.3.5. Re projection of the ROI complement (blue line) and the original projection (red line).

The subtraction of the complement ROI projection from the original projection will

give us the isolated ROI signal (figure 4.3.6) which will be used to perform the local ART reconstruction (Eq. 3.3.10) showed in the figure 4.3.7.

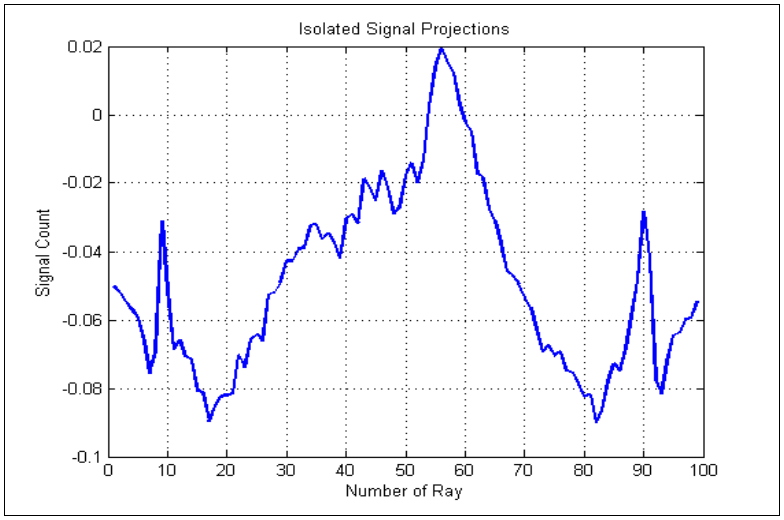

Figure 4.3.6. Isolated ROI signal: subtraction of the complement ROI projection from the original signal (referred to figure 4.3.5).

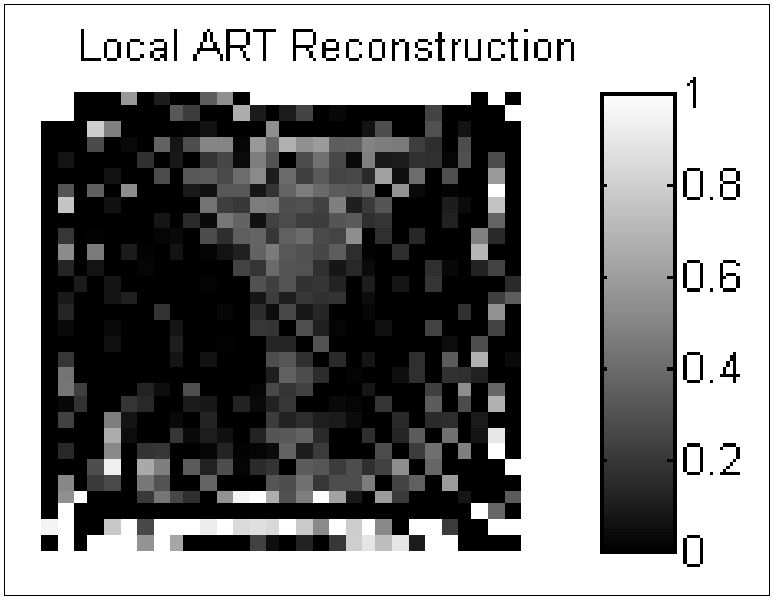

Figure 4.3.7. Local ART reconstruction with 15 iterations.

This last result was performed without noise management, an off-level problem in the first reconstructed image (figure 4.3.3) being the main cause. A method to correct for this error is explained in the next Chapter.

CHAPTER 5: RESULTS

In this chapter an analysis of the noise induced by the IRT-RT transform will pe performed and a modality to reduce its influence on the quality of the image will be presented.

5.1 Local Image with Leveling Corrections

The figure 4.3.3 of the previous section only suggested that using IRT-RT will result in projections which are off by a certain amount from the real image. Unfortunately, this off-displacement δ is not known in general, when the initial image is not known. Here it will be used as a parameter and we will try to find its best value for reconstruction purposes. This new parameter δ will be a subtraction or an addition of the FBP reconstructed image and this is the only correction performed. In general, for the FBP δ is a subtraction since written routines used in this work always produced a larger pixel value of the image reconstructed via FBP. A study for different values of the δ parameter was performed and was quantized via the correlation coefficient (Eq. 4.2.2) and the image error (Eq. 4.2.1). As a result, we found the optimal δ for which the maximum value of the correlation coefficient or the minimum value of the image error have been obtained. This procedure is presented in the figure 5.1.1 and magnified in the figure 5.1.2.

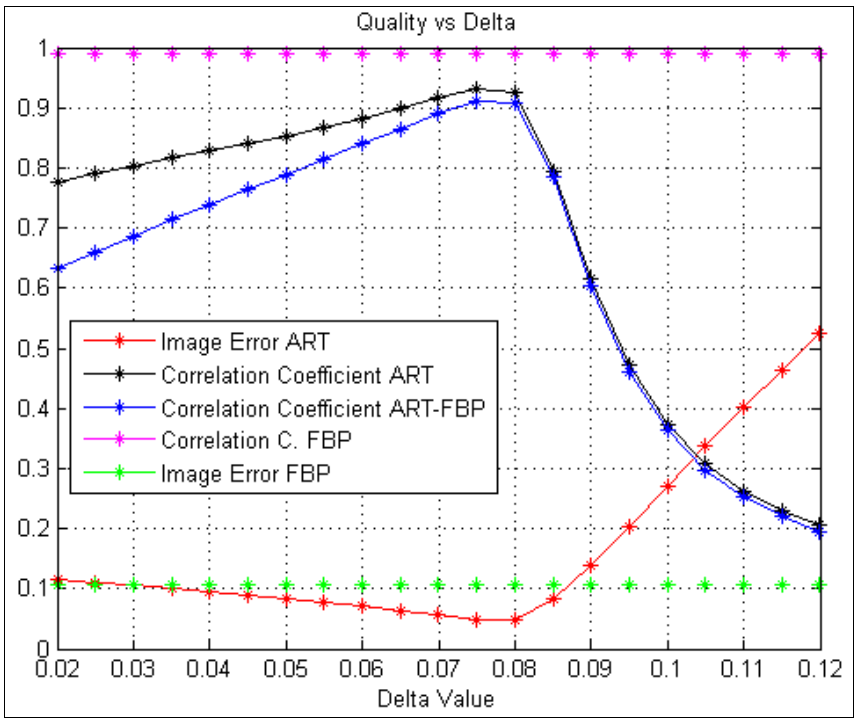

Figure 5.1.1. Image quality vs delta value for the local image reconstruction: Correlation Coefficient ART-Original image (black starred line) and C.C. ART-FBP (blue starred line).64 by 64 original image, 30 by 30 ROI size, 180 projection tomography image from 0º to 180º and 90 parallel rays per projection.

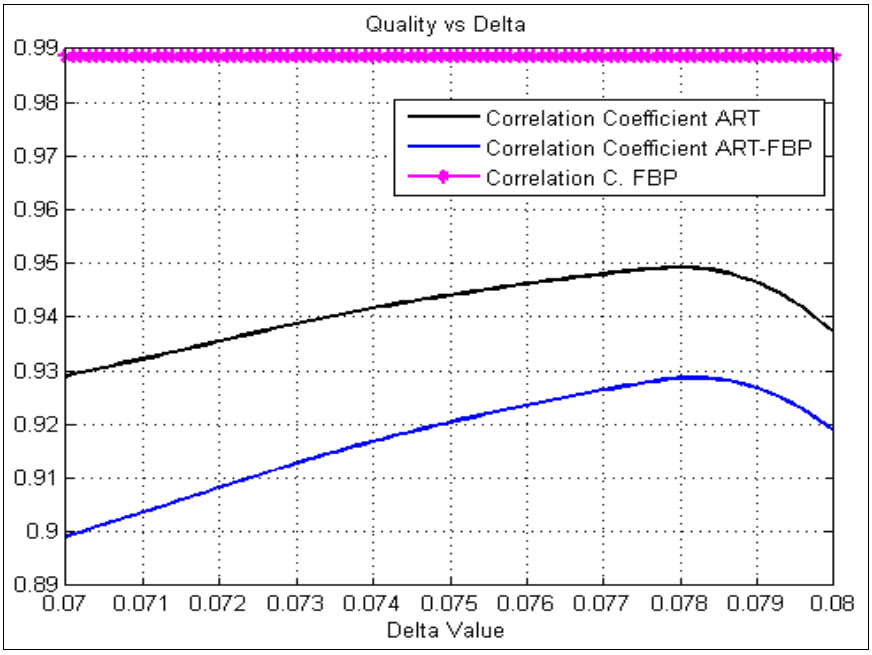

Figure 5.1.2. High resolution plot for the image quality (C.C.) vs delta.

From the figure 5.1.2 an optimum parameter was obtained with a value of $\delta = 0.078$ (ART Correlation Coefficient $ART_{CC} = 0.929$ and FFBP Correlation Coefficient $ART_{CC} = 0.989$). We use this value for the parameter δ for the hybrid method and the local reconstruction of the ROI with ART. A comparison between the ROI's projection from the original image and obtained from the FBP reconstructed image with the method described is showed in the figure 5.1.3 while the corresponding ROI ART reconstruction in the Figure 5.1.4.

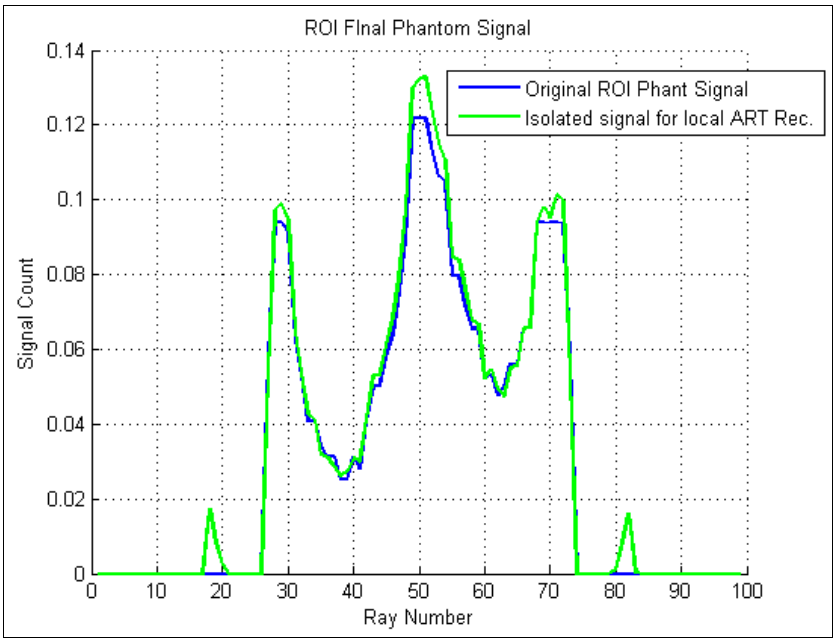

Figure 5.1.3. Comparative plots for the ROI signal after the leveling correction.

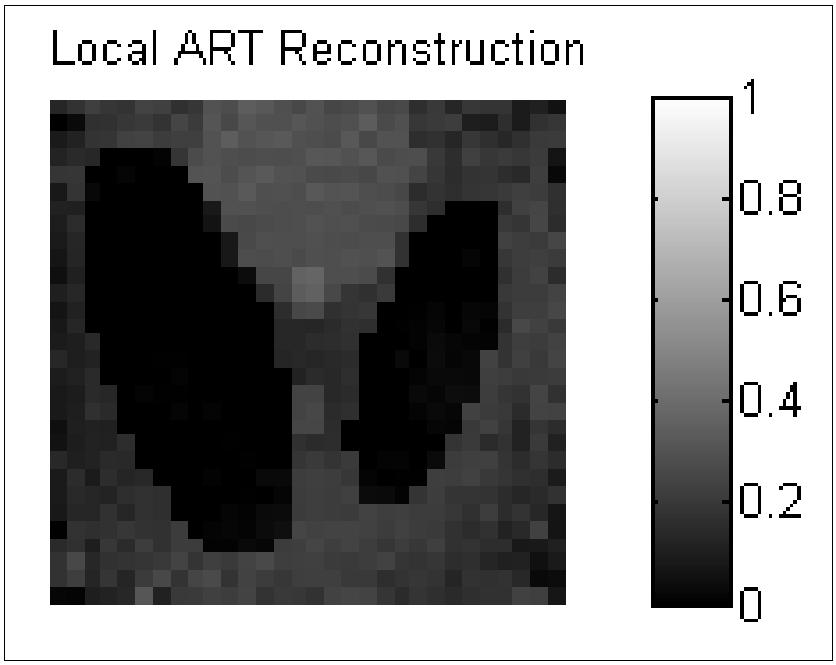

Figure 5.1.4. Final local ART reconstruction after the leveling correction.

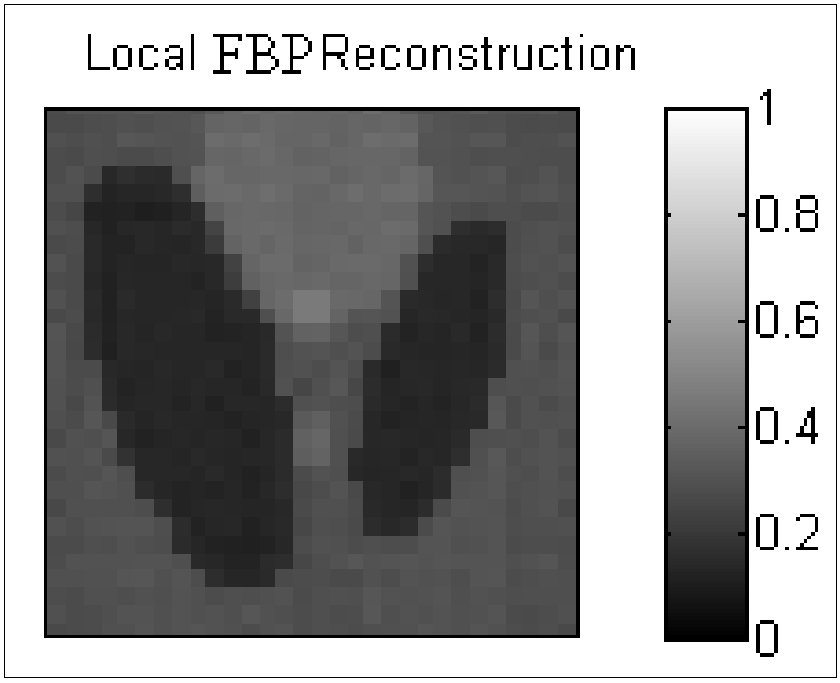

Figure 5.1.5. ROI for FBP reconstructed image.

5.2 Local Image Quality for Various Number of Projections

In this this section we will investigate how the hybrid method performs when only a subset of total projections are available. The image quality and the delta parameter are presented for various numbers of projections which are plotted in the figure 5.2.1.

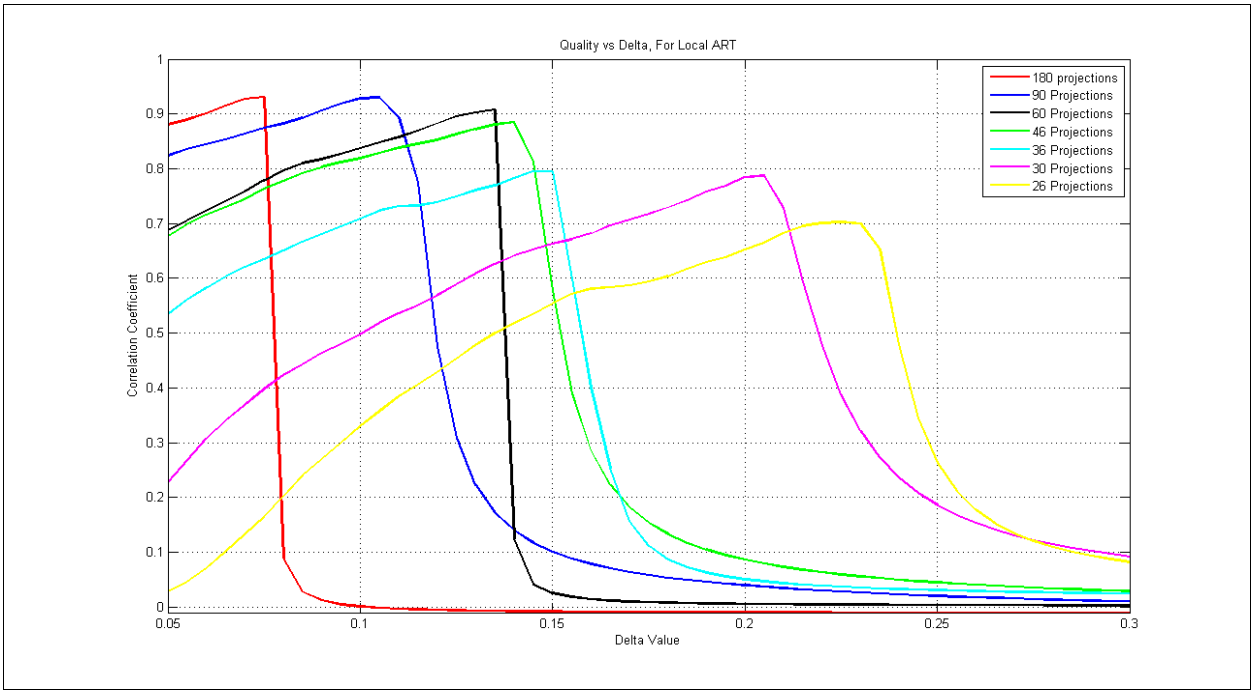

Figure 5.2.1. Image quality vs delta for different number of projections.

The optimal δ corresponding to the maximum value of each curve was used to draw a graph for optimum delta and Image quality vs the different number of projection for the ROI reconstructed with ART and FBP. This graphs are presented in the figure 5.2.2. and figure 5.2.3 respectively.

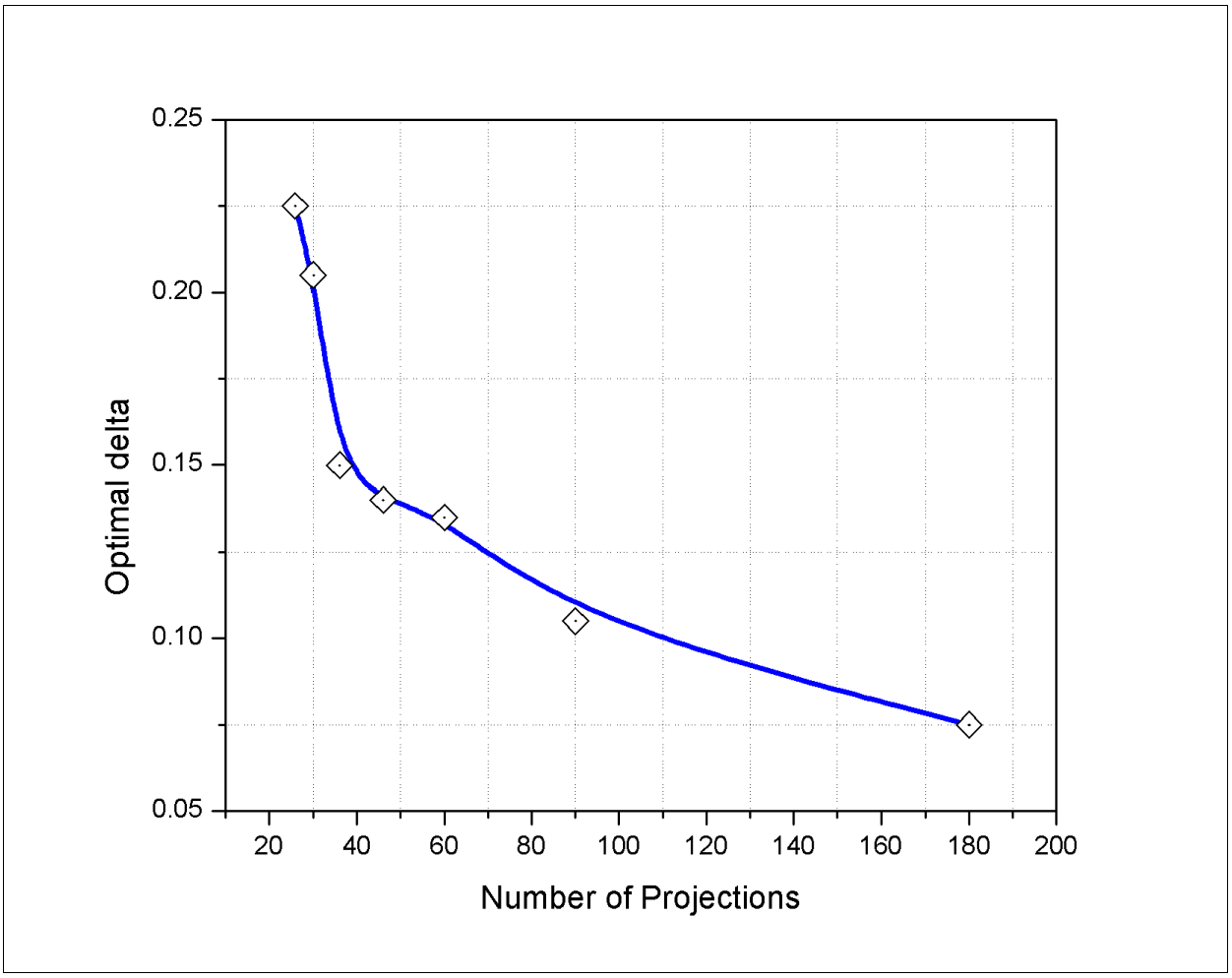

Figure 5.2.2. Optimum delta for the ROI vs number of projections for ART.

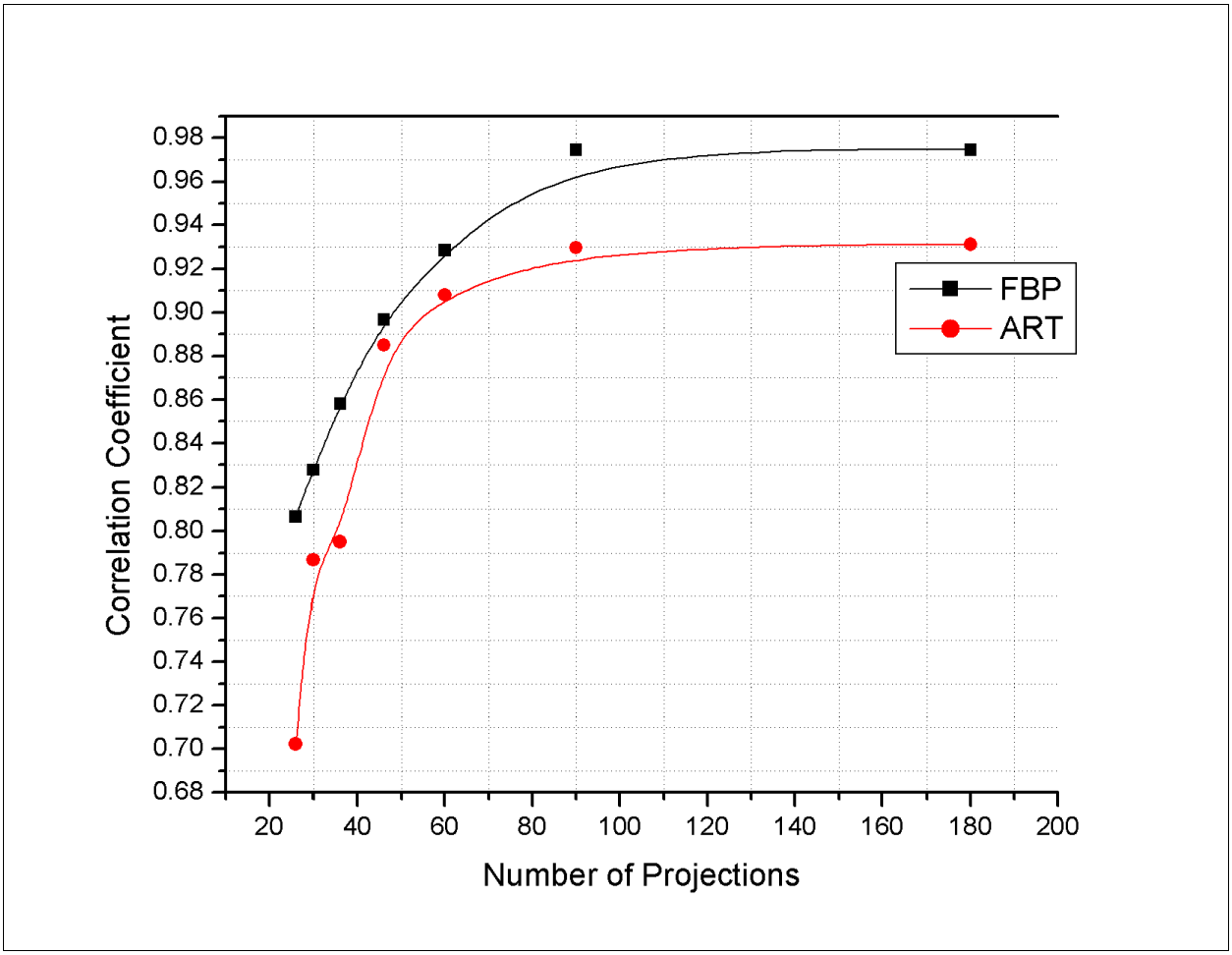

Figure 5.2.3. Image quality for the ROI vs number of projections for ART and FBP.

5.3 Local Image Quality with Quantum Noise

In order to know the behavior of the method when noise due to the quantum nature of light is present, the same analysis of section 5.2 was performed for three different levels of quantum noise.

The hybrid method and the image quality vs number of projections for the ROI reconstruction was performed with 1%, 2%, and 3% of quantum noise. Those graphs are shown in the figure 5.3.1.

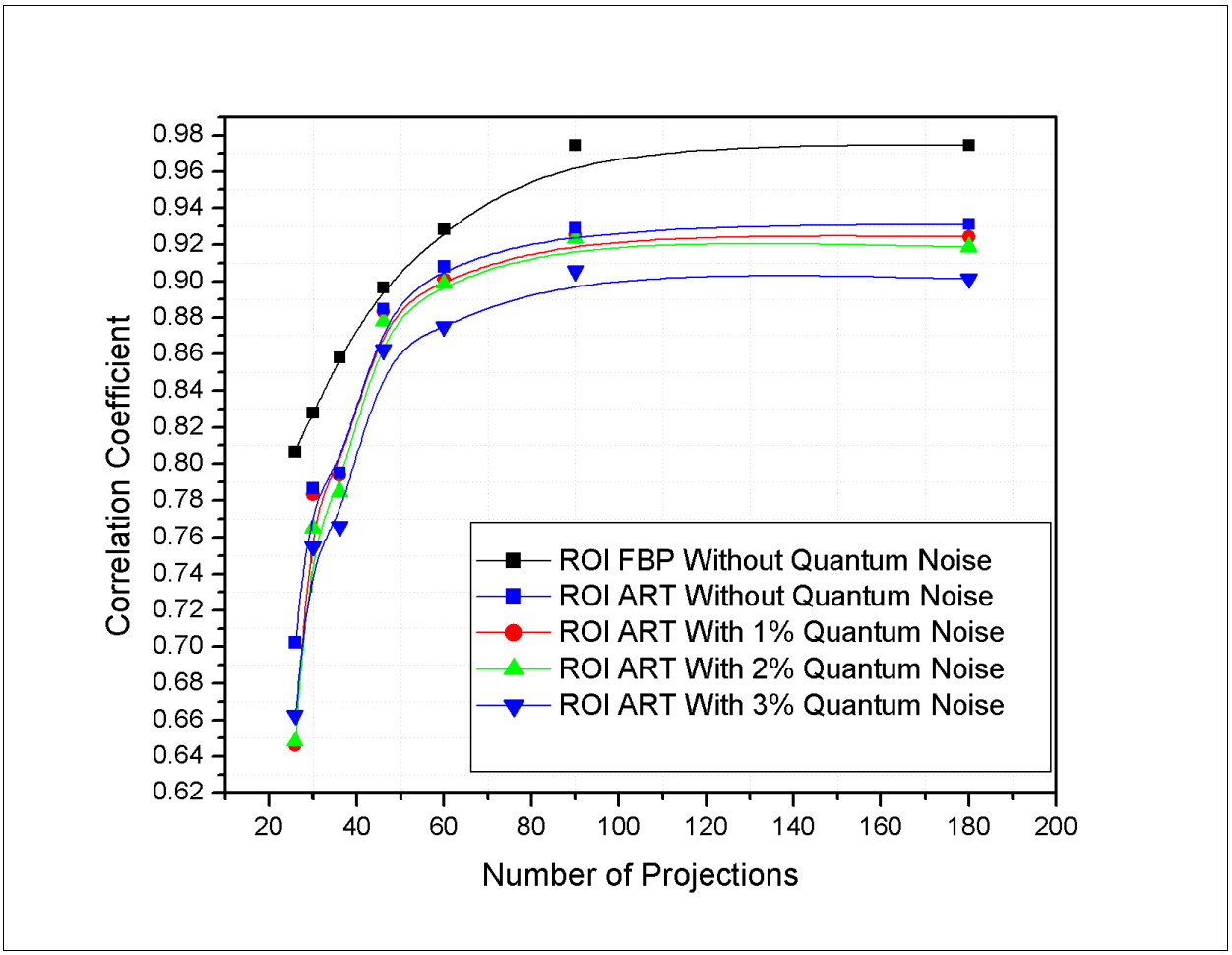

Figure 5.3.1. Image quality vs number of projections for the ROI reconstruction was performed with 1%, 2%, and 3% noise for ART and FBP.

5.4 Local Image Quality with Different sub Dimension Size

Finally, in this section the hybrid method is applied to ROI of different sizes: 10, 15, 20, 25, 30, and 35. I calculated the image quality vs ROI dimension size. This graph is presented in the figure 5.4.1.

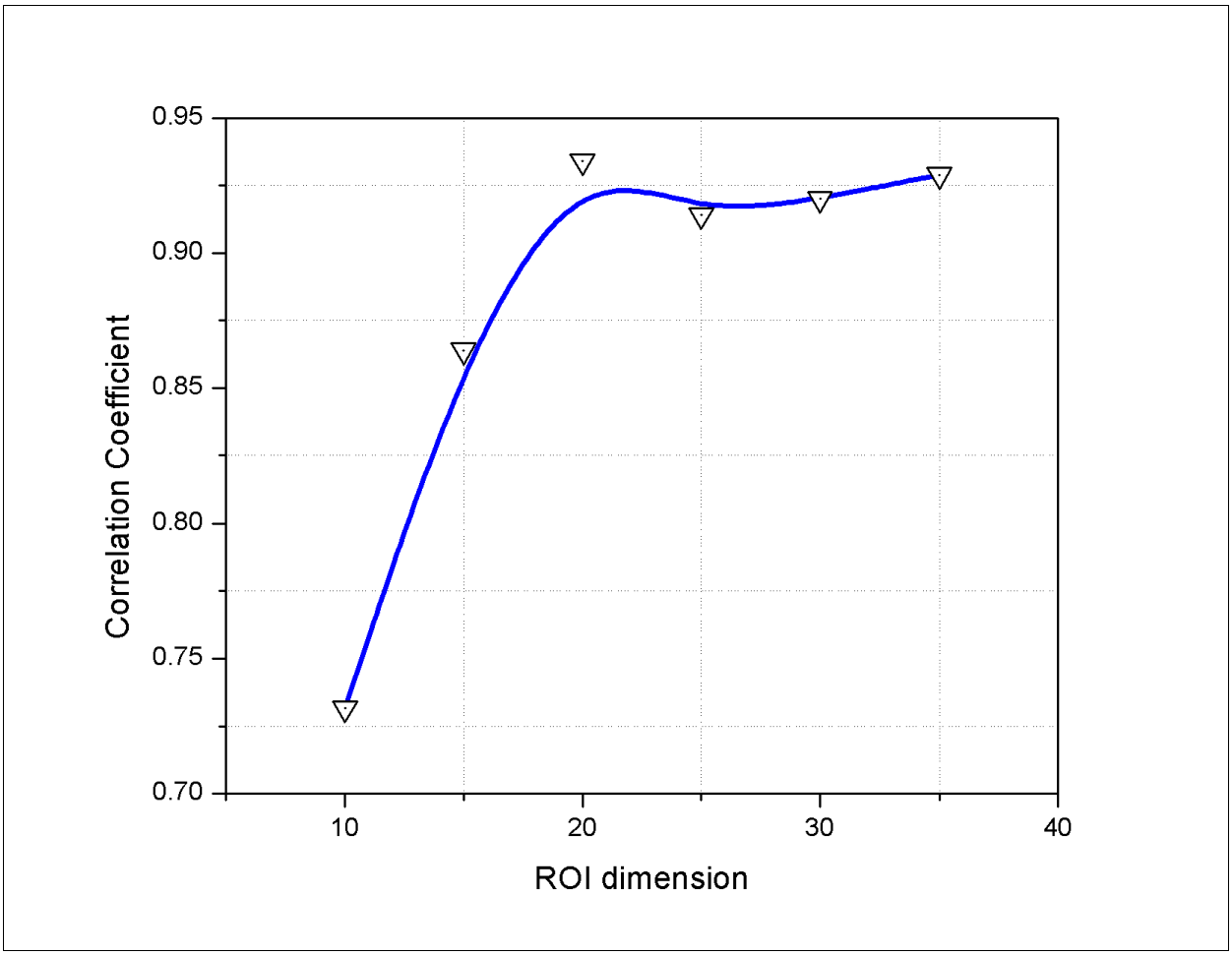

Figure 5.4.1. Image quality vs ROI dimension size.

CHAPTER 6: DISCUSSIONS AND CONCLUSIONS

6.1 Results and Discussion

The hybrid method, implemented with the two algorithms, ART and FBP, resulted in a poor quality reconstruction when a leveling correction is not performed. With the introduction of a new parameter δ, for leveling correction, the local ART reconstructed image improved (See figure 5.1.2, ART Correlation Coefficient ART_{CC} = 0.929) but not as good as the first reconstructed image from the FBP (FBP_{CC} = 0.989). On the other hand, the figure 5.1.4 show a better contrast rather than the ROI taken from the FBP reconstruction in the figure 5.1.5.

The figure 5.1.1 shows the quality of the local ART reconstructed image vs the value of δ, it is important to note that when the value is the optimum there is a maximum in the correlation coefficient value; the ART reconstructed image is leveled with the original image. This last statement is an important result because this parameter will show the real signal level of the image respect to the reconstructed image. This figure shows that when the parameter δ is greater than the gap between the original image value level (right side of the maximum for the CC plot) the error will increase faster than when this gap is smaller (left side of the maximum value of the CC This asymmetric behavior was also observed for different numbers of projections (see figure 5.2.1).

The figure 5.2.3 shows us the behavior of the Correlation Coefficients as functions of the number of projections. This figure shows that the CC for FBP is higher with a higher number of projections, and is the same for the CC for local ART. We should remember that the Local ART reconstruction is a function of the FBP, therefore, all the oscillatory noise from FBP are

transferred and oversampled to the local ART reconstruction (due to fact that many X-ray lines are going through a pixel; hence an error in a pixel value gets amplified) This effect might be stronger at lower number of projections in the figure 5.3.1.

Finally the study for the local reconstruction was performed with changing ROI's size as shown in the figure 5.4.1. It could be inferred that the quality of the image improves for larger ROI sizes.

6.2 Conclusions

In this work, I implemented a novel method that is based on obtaining good approximation of the partial projection of the region of interest from the total projections of the whole image. The method uses FBP to create an intermediate image on which a ROI is selected and the corresponding partial projections are calculated via Radon transform. A method to reduce the noise due to IRT-RT is proposed and we showed that good approximations of the partial projections could be obtained. Once the partial projections are known, a fast algebraic algorithm is used to reconstruct the ROI . We showed that the image quality of the local ART reconstruction decreases with the dimension of the ROI. A decline of the image quality exist also when quantum noise is present. The sensitivity to noise is greater in the image locally reconstructed with ART than FBP. Due to the dependency of the local ART reconstruction on the FBP, the noise is amplified in the local ART reconstruction. The behavior of the off leveled image signals affect negatively the local ART reconstruction as an asymmetric function. This negative impact is larger for a delta value above optimal level than for a delta value below optimal level. Finally, the number of coefficient for the linear system was successfully reduced,

therefore, a faster ART implementation for local reconstruction could be performed to find suspected abnormalities that are clinically important in thevROI.

Future work will be in the directions of using a variationea method for guess and correction such as a total variation study of J. Dahl, et al. [7] and a Bayesian tomographic reconstruction method [9] applied to the ART method. I will be looking forward to test this method, with real data, to support or discard.

LIST OF REFERENCES

1. W. Akram, S. Gee, C. Gamiz, C. Pan and J. Romberg, "Image Processing Using SPECT Analysis by The Five Fearless Thinkers," (1996).

2. M. Anastacio, D. Shi, X. Pan, C. Pelizzari and P. Munro, "A preliminary investigation of local tomography for megavoltage CT imaging," Med. Phys. Volume 30, pp. 2969-2980 (2003).

3. R. N. Bracewell and A. C. Riddle, "Inversion of Fan-Beam Scans in Radio Astronomy," Astrophysical Journal vol. 150 (1967).

4. R. N. Bracewell, Two-dimensional imaging. (Prentice-Hall, Inc, 1995).

5. J. T. Bushberg, J. A. Seibert, E. M. Leidholdt and J. M. Boone, The Essential Physics of Medical Imaging. (Lippincott Williams & Wilkins, 2002).

6. Z. Chen and R. Ning, "Filling the Radon domain in computed tomography by local convex combination," Applied Optics 42, 7043-7051 (2003).

7. J. Dahl, P. C. Hansen, S. Holdt Jensen and T. Lindstrøm Jensen, "Algorithms and software for total variation image reconstruction via first-order methods," Numerical Algorithms (2009).

8. T. Frese, C. A. Bouman and K. Sauer, "Multiscale Bayesian Methods for Discrete Tomography," in Discrete Tomography: Foundations, Algorithms and Applications, edited by E. b. G. T. H. a. A. Kuba (Birkhauser Boston, Cambridge, MA, 1999), pp. pp. 237-261.

9. T. Frese, N. C. Rouze, C. A. Bouman, K. Sauer and G. D. Hutchins, "Quantitative Comparison of FBP, EM, and Bayesian Reconstruction Algorithms, Including the Impact of Accurate System Modeling, for the IndyPET Scanner," IEEE Transactions on Medical Imaging vol. 22, pp. 258-276 (2003).

10. H. Guan, M. W. Gaber, D. F. A. and Y. Zhu, "CT reconstruction by using the MLS-ART technique and the KCD imaging system--I: low-energy X-ray studies.," IEEE Trans. Med. Imag. 18, 355-358 (1999).

11. H. Guan, "Comparison of the adaptive local tomographic reconstruction using the MLS-ART and the convolution back-projection (CBP) technique," in IFMBE Proceedings, Vol. Volume 14, (Springer Berlin Heidelberg, 2007), pp. 1365-1367.

12. H. Guan and R. Gordon, "A projection access order for speedy convergence of ART (algebraic reconstruction technique): a multilevel scheme for computed tomography," Phys. Med. Biol. 39, 2005-2022 (1994).

13. H. Guan, F.-F. Yin, Y. Zhu and J. H. Kim, "Adaptive portal CT reconstruction: A simulation study," Med. Phys. 27 (2000).

14. G. T. Herman, "Image Reconstruction from Projections: The Fundamentals of Computed Tomography," Med. Phys. Volume 9, pp. 446-448 (1982).

15. J. Hsieh, Computed Tomography: Principles, Design, Artifacts, and Recent Advances. (SPIE Press, 2003).

16. A. K. Jain, Fundamentals of digital image processing. (Prentice-Hall, Inc, 1989).

17. A. C. Kak and M. Slaney, Principles of Computerized Tomographic Imaging. (Society of Industrial and Applied Mathematics, 2001).

18. A. Katsevich and A. G. Ramm, The Radon Transform and Local Tomography. (CRC Press Inc., 1996).

19. J. H. Kim, B. Y. Choi and K. Y. Kim, "Novel Iterative Image Reconstruction Algorithm for Electrical Capacitance Tomography: Directional Algebraic Reconstruction Technique," IEICE Trans. Fundamentals Vol. E89-A, 1578-1584 (2006).

20. A. B. Konovalov, D. Mogilenskikh, V. V. Vlaslov and A. Kiselev, "Algebraic Reconstruction and Post-Processing in Incomplete Data Computed Tomography: From X-rays to Laser Beams," in Vision Systems: Applications, edited by E. b. G. O. a. A. Dutta (2007).

21. A. V. Lakshminarayanan, Reconstruction from divergent ray data. (State University of New York at Buffalo. Dept. of Computer Science. Technical report, 1975).

22. J. S. Lim, Two-Dimensional Signal and Image Processing. (1990).

23. E. J. Mazur and R. Gordon, "Interpolative algebraic reconstruction techniques witout beam partitioning for computed tomography," Med. & Biol. Eng. & Comput. 33, 82-86 (1995).

24. K. Mueller, Z. Liang, T. Li, F. Xu and e. al., presented at the IEEE Medical Imaging Conference (MIC) 2003, 2003 (unpublished).

25. K. Mueller and R. Yagel, presented at the IEEE MEdical Imagin Conference, 1998 (unpublished).

26. O.-S. Inc., "Beam Width Measurement Accuracy," (2009).

27. G. N. Ramanchandran and A. V. Lakshminarayanan, "Three dimensional reconstructions from radiographs and electron micrographs: application of convolution instead of Fourier transforms," Proc. National Acad. Sciences USA Vol. 68, pp. 2236-2240 (1971).

28. S. Smith, Universidad Fransisco Marroquin, 1986.

29. S. van der Maar, K. J. Batenburg and J. Sijbers, presented at the Liege Image Days 2008: Medical Imaging, 2008 (unpublished).

30. L. Vazquez, The University of Texas at El Paso, 2008.

31. J. Zheng, S. S. Saquib, K. Sauer and C. A. Bouman, "Parallelizable Bayesian Tomography Algorithms with Rapid, Guaranteed Convergence," IEEE Trans. on Image Processing Vol. 9, pp. 1745-1759 (2000).

APPENDIX A: RELEVANT CODES USED

List for Relevant *MatLab*® Codes Developed in this Work:

```
% Marco Antonio Barrera-Cruz
% University of Texas at El Paso
% MATLAB R2006a V7.2.0.232
% ART reconstruction
function [img] = ARTRec(NI,theta1,R,t,w);

load raycoord
load BPreconstruction

tic
% REMEMBER HERE MATRICES ARE (ROWS,COLUMNS)
 img= ones(NI,NI);
% img =BPimg ;


 for m = 1:t    %%

for i = 2:1:length(theta1)-1
       for j = 1:length(source)

       ww = matrixw(i,j,NI,w);  %% I took off the normalization on the
subroutine
       p =  vectorp(j,i,R);
       q = vectorq(NI,img,ww);
       w2 = vectorq(NI,ww,ww);
       if w2 ==0
           w2=1;
       end

       img = img + ((p-q)/w2)*ww;
       end

end
 ARTest(m) = vectorq(NI,img,img);
end
ARTimg=img;

toc

save('ARTreconstruction','ARTimg','ARTest');
```

A2

```
% Marco Antonio Barrera-Cruz
% University of Texas at El Paso
% MATLAB R2006a V7.2.0.232
%Filtered Backprojection Reconstruction, functions vectorp.m and vectorq.m
function [img] = BPRec(NI,theta1,R);

tic
%load weigthBP  %% matrix of zeros and ones.
load weigth
load raycoord

% REMEMBER HERE MATRICES ARE (ROWS,COLUMNS)

img =zeros(NI,NI);

R = filtersinc(R); %filtering with hiperbolic sine
for i = 1:1:length(theta1)-1
           for j = 1:length(source)

       p =  vectorp(j,i,R);
%       wbp(i,j,:,:) =p*wbp(i,j,:,:);
       w(i,j,:,:) =p*w(i,j,:,:);
%       ww = matrixw(i,j,NI,wbp);  %% I took off the normalization on the
subroutine
              ww = matrixw(i,j,NI,w);  %% I took off the normalization on the
subroutine
       img = img + ww;

       end

end
 %BPtest = vectorq(NI,img,img)

BPimg = img - min(min(img)); % Offset ( Eric Rodrigo)
BPimg = BPimg/max(max(BPimg));
toc

save('BPreconstruction','BPimg');
```

A3

```
function g = filtersinc(PR);

% filtersinc.m
%
% Written by Waqas Akram
%
% "a":  This parameter varies the filter magnitude response.
%   When "a" is very small (a<<1), the response approximates |w|
%   As "a" is increased, the filter response starts to
%   roll off at high frequencies.
a = 1;

[Length, Count] = size(PR);   %% [Length, Count] = [50,size(PR,2)];      %%%
modifique aqui
w = [-pi:(2*pi)/Length:pi-(2*pi)/Length];

rn1 = abs(2/a*sin(a.*w./2));
rn2 = sin(a.*w./2);
rd = (a*w)./2;
r = rn1*(rn2/rd)^2;

f = fftshift(r);
for i = 1:Count
        IMG = fft(PR(:,i));
        fimg = IMG.*f';
        g(:,i) = ifft(fimg);
end
g = real(g);
```

A4

```
% Marco Antonio Barrera-Cruz
% University of Texas at El Paso
% MATLAB R2006a V7.2.0.232
% Hybrid program with noise treatment.
%% GLOBAL VARIABLES

tic
set=[1, 3, 7, 15, 20, 25]; % number of folder for different parameters

for k=1:length(set)

folder(set(k))

load param
%load BPreconstruction
%load projection
load weigth
np(k)=length(theta1);
a=yi;b=xi;I4=phantom(NI);
[R,Q]=projection(I4);
BPimg=BPRec(NI,theta1,R);
%
subBPimg=zeros(sld,sld);
subphant=zeros(sld,sld);
s1=1;
s2=1;
for i=a:1:a + (sld-1);
for j=b:1:b + (sld-1);
subBPimg(s1,s2)=BPimg(i,j);
subphant(s1,s2)=I4(i,j);
s2=s2+1;
end
s2=1;
s1=s1+1;
end
save('subimages','subBPimg','subphant');

%load subimages
%Statistic
nulo=ones(sld,sld);
mu1 = vectorq(sld,subphant,nulo);
mu2 = vectorq(sld,subBPimg,nulo);
mu1a=mu1/(sld*sld);%original average
mu2bp=mu2/(sld*sld);%BP average
ieBP    = imageerror(subBPimg,subphant,sld);
ccBP  = correlation(subphant,subBPimg,sld,mu1a,mu2bp);
delta = 0.05:0.01:0.2; %% finding DELTA

 for m =1:length(delta)
    tic

I2=BPimg;
I2=I2 - delta(m);  %%%% this is the
```

A5

```
KEY !!!!!!!!!!!!!!!!!!!!!!!!!!!!!!!!!!!!!!!!
for i=1:NI                      %FILTER for Back projection
for j=1:NI
    swap=I2(i,j);
    if swap < 0.0
    swap=0;
    end
   I2(i,j)=swap;
end
end

%% CUT
a=yi;
b=xi;% +sld;
I3=I2;
for i=a:1:a + (sld-1);
for j=b:1:b + (sld-1);
    I3(i,j)=0;
end
end
% figure, imshow(I3);
%% RE-PROJECTING

[R1,Q1]=projection(I3);

R2=R-R1;    %% projections Subtraction
swap=0;
e2=size(R2);
for i=1:e2(1)                   %FILTER for Back projection
for j=1:e2(2)
    swap=R2(i,j);
    if swap < 0
    swap=0;
    end
   R2(i,j)=swap;
end
end
%% Local Reconstruction
t2=10;
 subARTimg = subARTRec(xi,yi,sld,NI,theta1,R2,t2,w);
%% Statistics
 mu2 = vectorq(sld,subARTimg,nulo);
mu2a=mu2/(sld*sld);%BP average

ieART  = imageerror(subARTimg,subphant,sld);
ccART  = correlation(subphant,subARTimg,sld,mu1a,mu2a);
ccBOTH = correlation(subARTimg,subBPimg,sld,mu1a,mu2bp);
results(k,m,1)=delta(m);
results(k,m,2)=ieART;
results(k,m,3)=ccART;
results(k,m,4)=ccBOTH;
results(k,m,5)=ieBP;
results(k,m,6)=ccBP;
```

A6

```
toc
end %end for m

cd ..
save('StatResults','results','np');
end
toc
```

A7

```
% Marco Antonio Barrera-Cruz
% University of Texas at El Paso

function [ww] = submatrixw(i,j,xi,yi,sld,NI,w);

%% getting matrix of weights
ww = zeros(sld,sld);

a=yi;
b=xi;

s1=1;
s2=1;
for l=a:1:a + (sld -1);
s2=1;

for k=b:1:b + (sld -1);
ww(s1,s2) = w(i,j,l,k);
s2=s2+1;
    end
    s1=s1+1;
end

% Marco Antonio Barrera
% University of Texas at El Paso


function [w2] = wdotw(n,w);
swap = zeros(n,n);

swap = dot(w,w,n);
w2 =0;
for l = 1:n
    for k= 1:n

w2 = w2 + swap(l,k);

    end
end
```

A8

```
% Marco Antonio Barrera-Cruz
% University of Texas at El Paso
% MATLAB R2006a V7.2.0.232
% parameters  'param.m'

clear all, close all, clc

NI=64; % IF YOU CHANGE HERE, YOU HAVE TO CHANGE ON FILE Tomo1
st=1.0;
theta1 = [0:st:88,92:st:180];%:5:85,95:5:175]; %,182:2:268,272:2:358]; %angle
of prejections for PARALLEL BEAM, DEGREES {avoiding 90 & 270}
nr =99; % number of sources or rays off of the zero
lr=sqrt(2);
source = [-(0 + lr/nr:lr/nr:lr*0.5),0, 0 + lr/nr:lr/nr:lr*0.5]; % Ray sources
source = sort(source);
mm = [-(1:(nr/2)),0,1:(nr/2)];  %ray numerator
mm=sort(mm);
xi=18;
yi=18;
sld=30;
t1=1;
t2=20;
%delta=0.0785;
save('param','NI','theta1','nr','xi','yi','sld','t1','t2'); %,'delta');
```

A9

```
%% First code of tomography "projection.m"
% Marco Antonio Barrera-Cruz
% University of Texas at El Paso
% MATLAB R2006a V7.2.0.232
function [R,Q]=projection(phant)
tic
%clear all
 %clc

load lttcoord
load param
load raycoord
load weigth

%phant = phantom1(NI);
% run origimage

%%

for i=1:length(theta1)
    for s = 1:length(source)
       ww = matrixw(i,s,NI,w);  %% I took off the normalization on the
subroutine
%        ww =(sqrt(2)/NI)*ww;
       q = vectorq(NI,phant,ww);
       R(s,i) = q;                          %% Vector RAdon of Signal
Here i changed R(i,s)-->R(s,i) 03/16/2009
       Q(s,i) = awgn(q,45);   %% Vector RAdon of Signal Adding Noise

end
end

clear y inth2;

toc
```

A10

```
%% First code of Tomography "Tomo1.m"
% Marco Antonio Barrera-Cruz mabarrera@miners.utep.edu
% University of Texas at El Paso
% MATLAB R2006a V7.2.0.232
%%
% clc, clear all, close all,

%% Parameters
tic
% NI=16; % NI is a scalar that specifies the number of rows and col. in the
phantom. (size)
%nr =ceil(NI*sqrt(2)); % number of sources or rays off of the zero
%theta1 = [0:3:180];  %,182:2:268,272:2:358]; %angle of prejections for
PARALLEL BEAM, DEGREES {avoiding 90 & 270 for zeros singularities}
toc
%% lattice coordinates
tic
lttx = zeros(NI+1,1); % X coordinates of lattice, we have to remember that in
the lattice there are NI+1 lines and NI pixels on X direction.
ltty = zeros(NI+1,1); % Y coordinates of lattice
na = 1/NI;  % step size for lattice coord.
for i = 1: NI + 1;

    kk = -0.5 + (i-1)* na;
    lttx(i) = kk;
    ltty(i) = kk;

end

clear i na kk

save('lttcoord','lttx','ltty');
%save('param','NI','theta1','nr');

toc
%% Ray coordinates
tic
% source = [-0.5:1/nr:0 - 1/nr,0, 0 + 1/nr:1/nr:0.5]; % Ray sources
% mm = [-nr/2:-1,0,1:nr/2];
theta2 = 90 - theta1;
m = tand(theta1);
inth1 = zeros(length(source),length(ltty));
inth2 = zeros(length(theta1),length(source),length(ltty));

for i =1:1:length(theta1)
    for j = 1:length(source)

        bb = mm(j)*abs(1/(nr*sind(theta2(i))));
        ordenadas(i,j) = bb;

        if m(i) ==0
            inth1(j,:)=0*ltty;
        else
```

A11

```
        inth1(j,:) = (ltty - bb) /m(i);
        end

        y(i,j,:) = [m(i)*lttx + bb];

    end
inth2(i,:,:) = inth1;
    clear j k ll inth1;

end


%% Test plot of all the rays.
% for i = 1:1:length(theta1);
%
% for j =1:length(source)
%         figure(2)
%         for k = 1:length(lttx)
%             yp(1,k)=y(i,j,k);
%         end
%
%     plot(lttx,yp,'blue');
%     axis([-0.5 0.5 -0.5 0.5]);
%     grid on
%     hold on
%
% end
%
% end

clear mm i theta2
save('raycoord','y','source','ordenadas','inth2','m');
toc
```

A12

```
%% First code of tomography "Tomo2.m"
% Marco Antonio Barrera-Cruz
% University of Texas at El Paso
% MATLAB R2006a V7.2.0.232
%% Computing the length's intersections between rays and lattice coordinates.
clc, clear all, close all,
tic
load raycoord; load lttcoord; load param;
inth3=zeros(1,length(lttx));
inth4=zeros(1,2*length(lttx));
yp= zeros(length(theta1),length(source),2*length(lttx));
inth5= zeros(length(theta1),length(source),2*length(lttx));
%% gettin intersections

for i = 1:length(theta1)  %% ANGLE

        for j=1:length(source) %% SOURCE

        inth3(1,:)= y(i,j,:);                %%%  inth2(i,j,:);  I'm modifying
this rutines for the intersection on X to Y

            for ll=1:length(ltty)
                inth4(ll)= inth3(1,ll); %%% horizontal intersection
            end
            clear ll;
            for ll= length(ltty) + 1 :2*length(ltty)
            inth4(ll) = ltty(ll-length(ltty)); %%% Horizontal plus Vertical
intersecton
            end

        clear ll;

        inth5(i,j,:) = sort(inth4);    % inth4;     %%NOW THIS RUTINE IS ON "Y"
coord.

    end
end


clear inth2 inth3 inth4 i j bb


save('sets','inth5');
toc
%%
```

A13

%% First code of tomography "Tomo3.m"

```
% Marco Antonio Barrera-Cruz
% University of Texas at El Paso
% MATLAB R2006a V7.2.0.232
%% Computing the weigth of the line into the pixel
clear all; close all; clc;
load sets; load raycoord; load lttcoord; load param;

tic
w = zeros(length(theta1),length(source),NI,NI);   %%% CHECK this, i did from
NI to NI+1
tic
for i =  2 : length(theta1) -1
    for j = 1 : length(source)
        for k = 1 : (2*length(lttx) -1)

    yy1 = inth5(i,j,k);
    yy2 = inth5(i,j,k + 1);
    xx1 = (yy1 - ordenadas(i,j))/m(i);
    xx2 = (yy2 - ordenadas(i,j))/m(i);


    if (abs(xx1) <=  0.5) & (abs(xx2) <= 0.5) & (abs(yy1) <= 0.5) & (abs(yy2)
<= 0.5)  %% you have to modify this because "inth5" is no filtered
    aa = xx1 - xx2;
    bb = yy1 - yy2;

    [f,g] = coordenada(xx1,xx2,yy1,yy2,lttx,ltty);%% find coord
      w(i,j,f,g) = sqrt(aa^2 + bb^2); %weigth of a ray on pixels
    end

        end
    end
end
save('weigth','w');
toc
%  Plot for testing
%  i = 10
% for j =1:NI+1
%         figure(2)
%         for k = 1:length(lttx)
%             yp(1,k)=y(i,j,k);
%         end
%         ko1 = KOSA1(i,j,lttx,m,inth5,ordenadas);
%         ko2 = KOSA2(i,j,lttx,m,inth5);
%     plot(lttx,yp,'blue')
%     plot(ko1,ko2,'* red');
%     axis([-0.5 0.5 -0.5 0.5]);
%     grid on
%     hold on
% end
clear all;
```

A14

```
% Marco Antonio Barrera-Cruz
% University of Texas at El Paso
% MATLAB R2006a V7.2.0.232

function [p] = vectorp(i,j,R);

p=R(i,j);
---
function [q] = vectorq(n,img,ww);
swap = zeros(n,n);

swap = dot(img,ww,n);
q =0;
for l = 1:n
    for k = 1:n

q = q + swap(l,k);

    end
end

---


function [w2] = wdotw(n,w);
swap = zeros(n,n);

swap = dot(w,w,n);
w2 =0;
for l = 1:n
    for k= 1:n

w2 = w2 + swap(l,k);

    end
end
```

A15

RESUME

Marco Antonio Barrera-Cruz
e-mail: mabarrera@miners.utep.edu

Marco A. Barrera was born in October 15th of 1983 in the city of *Minatitlán, Veracruz, México*. He is second son of Amalia Cruz and Fredy Barrera. Marco started interest in science while he was pursuing his studies of high school with the Young Association for Divulgation of Science (AJDIC AC). In August of 2001 he started his bachelor degree in physics at the Autonomous University of Baja California. During his college years he work in several research projects: Numerical Simulation for Super Novas (CRyA-UNAM 08/2005); Stress-Induced DNA Duplex Destabilization (IFC-UNAM, 08/2006); and Tomography and Spectroscopy of Lab. Plasma (CCMC-UNAM 2007). Also he was President of the Students for College of Science (2006-2007) and General University Campus Alumni Governor (2007). Marco got his bachelor degree in physics by July of 2007. For the Fall of 2007 he started his M.S. In physics at the University of Texas at El Paso. He also was the Vice-President of the SPS UTEP chapter and was honored with the *Best Graduate Student Award* (2009) of the Physics Department.

This thesis was typed by Marco A. Barrera.